AD-A129 490   ANALYSIS OF INTERIOR BALLISTICS PROCESSES OF BULK   1/1
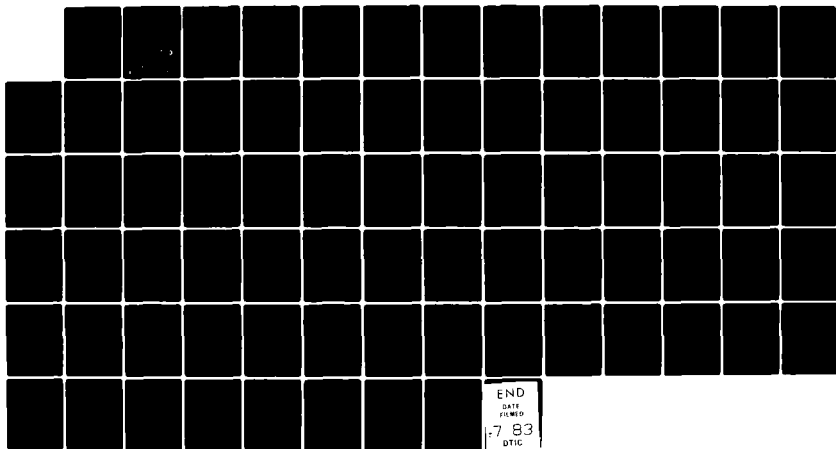   LOADED LIQUID PROPELLAN..(U) SCIENCE APPLICATIONS INC
              CHATSWORTH CA COMBUSTION SCIENCE AND..
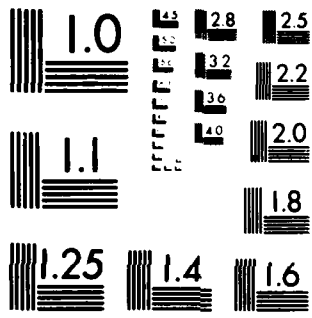UNCLASSIFIED R B EDELMAN ET AL. MAY 83 SAI-83-048-CH   F/G 19/1   NL

END
DATE
FILMED
7 83
DTIC

MICROCOPY RESOLUTION TEST CHART

NATIONAL BUREAU OF STANDARDS 1963 A

ANALYSIS OF INTERIOR BALLISTICS PROCESSES
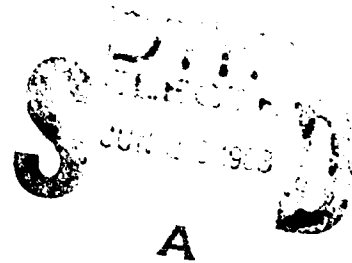OF BULK LOADED LIQUID PROPELLANT GUNS

Final Report

R. B. Edelman, G. Phillips and T. S. Wang

May 1983

U. S. ARMY RESEARCH OFFICE

Contract Number DAAG29-80-C-0028

Science Applications, Inc.
Combustion Science and Advanced Technology Department
9760 Owensmouth Avenue
Chatsworth, CA 91311

A

APPROVED FOR PUBLIC RELEASE;
DISTRIBUTION UNLIMITED.

THE VIEW, OPINIONS, AND/OR FINDINGS CONTAINED IN THIS REPORT
ARE THOSE OF THE AUTHORS AND SHOULD NOT BE CONSTRUED AS AN
OFFICIAL DEPARTMENT OF THE ARMY POSITION, POLICY, OR DECISION,
UNLESS SO DESIGNATED BY OTHER DOCUMENTATION.

REPORT DOCUMENTATION PAGE		READ INSTRUCTIONS BEFORE COMPLETING FORM
1. REPORT NUMBER	2. GOVT ACCESSION NO. AD-A129 190	3. RECIPIENT'S CATALOG NUMBER
4. TITLE *(and Subtitle)* Analysis of Interior Ballistics Processes of Bulk Loaded Liquid Propellant Guns		5. TYPE OF REPORT & PERIOD COVERED Final 1 Dec. 1979 - 15 Jan. 1983
		6. PERFORMING ORG. REPORT NUMBER 83-048CH
7. AUTHOR(s) R.B. Edelman, G. Phillips and T.S. Wang		8. CONTRACT OR GRANT NUMBER(s) DAAG29-80-C-0028
9. PERFORMING ORGANIZATION NAME AND ADDRESS Science Applications, Inc. 9760 Owensmouth Avenue Chatsworth, California 91311		10. PROGRAM ELEMENT, PROJECT, TASK AREA & WORK UNIT NUMBERS
11. CONTROLLING OFFICE NAME AND ADDRESS U. S. Army Research Office Post Office Box 12211 Research Triangle Park, NC 27709		12. REPORT DATE May 1983
		13. NUMBER OF PAGES
14. MONITORING AGENCY NAME & ADDRESS*(If different from Controlling Office)* U.S. Army Ballistics Research Laboratory Aberdeen Proving Ground Maryland 21005		15. SECURITY CLASS. *(of this report)* Unclassified
		15a. DECLASSIFICATION/DOWNGRADING SCHEDULE

16. DISTRIBUTION STATEMENT *(of this Report)*

Approved for public release; distribution unlimited.

17. DISTRIBUTION STATEMENT *(of the abstract entered in Block 20, if different from Report)*

Approved for public release; distribution unlimited.

18. SUPPLEMENTARY NOTES

The view, opinions, and/or findings contained in this report are those of the author(s) and should not be construed as an official Department of the Army position, policy, or decision, unless so designated by other documentation

19. KEY WORDS *(Continue on reverse side if necessary and identify by block number)*

Guns	Chemical Kinetics	Atomization
Liquid Propellants	Turbulence	Monopropellants
Multiphase Flow	Wave Dynamics	
Spray	Transient Combustion	

20. ABSTRACT *(Continue on reverse side if necessary and identify by block number)*

A transient two-dimensional turbulent reacting multiphase flow model has been developed for the analysis of the interior ballistics process in liquid propellant guns. The analysis accounts for finite rate vaporization and heat release at the liquid-gas interface and predicts the observed evolution of the Taylor cavity through the propellant. Comparisons between predictions and available data show agreement with observed trends in the pressure-time trace. Analysis of the results show that turbulent transport controls the combustion

DD FORM 1473 EDITION OF 1 NOV 65 IS OBSOLETE

20.

process during all phases of the firing cycle and that chemical kinetics is most critical to flame initiation. Preliminary analysis of the effects of droplet formation at the liquid-gas interface compared with direct liquid-to-gas conversion shows that the formation and consumption of droplets can result in more rapid burning and larger amplitude pressure oscillations. These results indicate that the overall combustion process is initiated.

TABLE OF CONTENTS

LIST OF TABLES

i

LIST OF FIGURES

LIST OF FIGURES (continued)

SUMMARY

Statement of the Problem Studied

The combustion of liquid propellants in experimental bulk loaded
liquid propellant gun fixtures has exhibited erratic behavior manifested in
shot-to-shot variability in the observed pressure-time measurements. A
theoretical analysis was undertaken to delineate the physical and chemical
mechanisms responsible for the observed behavior. The analysis is structured
to help understand the controlling parameters and to provide a base of
information relevant to the design and optimization of liquid propellant
guns.

Results

A transient, two-dimensional, multiphase, turbulent reacting flow
model was formulated and implemented for digital computations. This model
accounts for finite rate vaporization and heat release at the liquid-gas
interface and predicts the observed evolution and propagation of the Taylor
cavity through the propellant.

Comparisons between predictions and available data show agreement
with the observed trends in the pressure-time trace. The predicted results
include details of the reacting flow that have not been measured. These
results have provided insights on the relative sensitivity of the combus-
tion process to certain of the physical and chemical mechanisms. Analysis
of these results show that turbulent transport controls the combustion
process during all phases of the combustion process and that chemical
kinetics is most critical to flame initiation which, in turn, affects the
pressure-time characteristics during the remainder of the combustion process.
In addition, preliminary analysis of the effects of droplet formation at
the gas-liquid interface compared with direct liquid-to-gas conversion
shows that the formation and consumption of droplets can result in more
rapid burning and larger amplitude pressure oscillations.

These results are significant because they indicate that the
overall combustion process is strongly dependent upon the way the combustion
process initiates. Therefore, future research should concentrate on three

main areas: propellant physical properties and their effects on the evolution
of turbulence and droplet formation; propellant reactivity with emphasis on
the rate of initiation of decomposition, and the propellant injection
process including an examination of swirl as a means of controlling the
initial flow pattern and mixing rate.

ANALYSIS OF INTERIOR BALLISTICS PROCESSES
OF BULK LOADED LIQUID PROPELLANT GUNS

SECTION I
INTRODUCTION

Liquid propellant guns (LPGs) represent a concept in gun design that offers many advantages over conventional solid propellant weapons. Higher impulses at lower peak pressures, cooler operation, reduced erosion, improved propellant management and the elimination of the cartridge are the major advantages, all of which lead to a light weight, low-volume gun system that is capable of high muzzle velocities at sustained rates of fire. Certain of these advantages have been demonstrated in laboratory-type hardware. However, cases have been reported in which unacceptable pressure-time traces have occurred. Shot-to-shot variability has been the major concern and the interpretation of pressure-time traces to help understand how to control the process has been hampered by the complexity of the liquid propellant combustion process.

The LPG interior ballistics process is unique and can perhaps be best illustrated by contrasting it with its solid propellant counterpart. In the case of solid propellants, the burning surface is relatively well defined and remains so during the firing cycle. With liquid propellants, however, the liquid itself enters into the fluid dynamic process and because of the acceleration of the liquid and the relative velocity between the products of combustion and the propellant, both Taylor and Helmholtz instabilities can occur. [1]. These can lead to the important phenomena of cavity and liquid droplet formation and turbulent mixing. Thus, the burning surface in the LPG is intimately coupled to the details of the reacting flowfield as it develops during the firing cycle. In fact, the effective burning surface area can be several orders of magnitude greater than an area based upon the chamber cross-section. Thus, the process is relatively complex since it involves strong coupling between fluid dynamic and chemical mechanisms under highly transient,

1

multiphase flow conditions. In spite of this complexity, preliminary studies were successful in delineating certain of the mechanisms controlling the interior ballistics process [2]. Although the model described in Reference 2 is a global one based upon spatially averaged properties, it nevertheless showed that the overall combustion process is sensitive to the early-time behavior, i.e., the ignition process. Moreover, it was demonstrated that turbulent mixing plays a dominant role in controlling the combustion process at all stages of the firing cycle.

These studies have suggested that chemical kinetics and possibly droplet formation and consumption processes at the liquid/gas interface could play important roles particularly during ignition and the early flame development stages. While the model described in Reference 2 has provided some important insight into the interior ballistics process, it is not a predictive tool. In fact, like other published models of the LPG interior ballistics process [3,4], it is based in part on having empirical information available and in part on preconceived notions; the existence of a "Taylor Cavity" is assumed a priori. The model described in this report provides an analytical description of all of the major and chemical processes which occur within the LPG, and thus it is intended, with suitable development, to be a predictive tool. Chemical kinetics, turbulence, and droplet formation and consumption processes at the liquid/gas interface are all incorporated in the approach. Although, because of the limited data available, some of the analytical submodels incorporated in this LPG model must be parameterized, the approach offers considerable promist for development as a tool to aid in the interpretation of experimental data on the LPG interior ballistics process.

SECTION 2
THE NATURE OF THE LPG COMBUSTION PROCESS

Figure 1 depicts the principal phases encountered during a complete firing cycle. Figure 1(a) shows the injection process that serves to fill the chamber and seat the projectile while also providing a highly dynamic environment that creates a level of residual turbulence. Figure 1(b) shows the state in the propellant at the moment of ignition.

After injection is complete, the projectile is seated and the system is in the ready-to-fire configuration, Figure 1(b) Immediately following the ignition process, a complex fluid dynamic/chemical process initiates. The energy deposited into the propellant will cause the propellant to heat up, vaporize, and decompose. The pressure will rise and initiate motion in the propellant. The motion will include wave propagation and turbulence generated by Taylor-Helmholz instabilities that arise from the accelerating force acting across the vapor liquid interface (residual turbulence from the dynamics of the injection process will also augment the mixing process). The decomposition process involves the formation of highly reactive intermediates which, upon reaching a critical level of concentration, will react exothermically and ultimately form the final products of combustion. The period during which the "reactive" species are formed is analogous to the classical "ignition delay" time which is reflected in the pressure trace as a relatively constant, low pressure regime. This time period, prior to the development of sustained combustion, involves a balance between the rate of energy deposition in the affected volume of propellant, the rate of formation and exothermic combination of the "reactive" species and the rate of mixing with fresh propellant. If no new propellant is added to the initial volume, the reaction will not proceed. However, if the rate of entrainment of new propellant into the initial reaction volume is too great, the reaction may also be quenched or critically delayed until a relatively large volume of highly reactive species combine explosively. Thus, this early time control of the chemical kinetics and fluid mechanics is crucial to smooth ignition and development of sustained burning.

a) FILLING PROCESS

- PRECOMBUSTION CHAMBER
- PROPELLANT
- PROJECTILE
- PROPELLANT

b) READY-TO-FIRE

RESIDUAL TURBULENCE

c) IGNITION PROCESS

JET INTERACTION, ENTRAINMENT, MIXING & CHEMISTRY
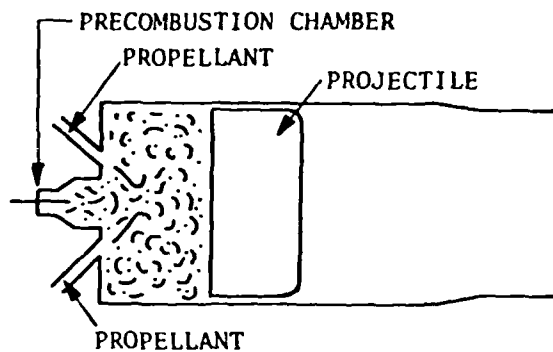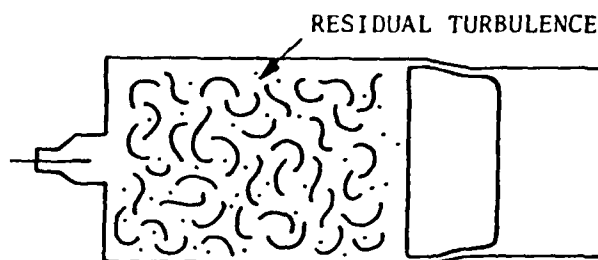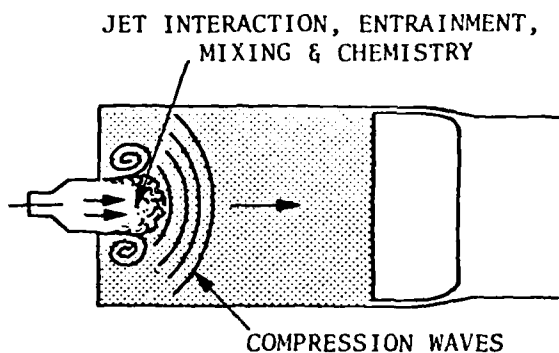
COMPRESSION WAVES
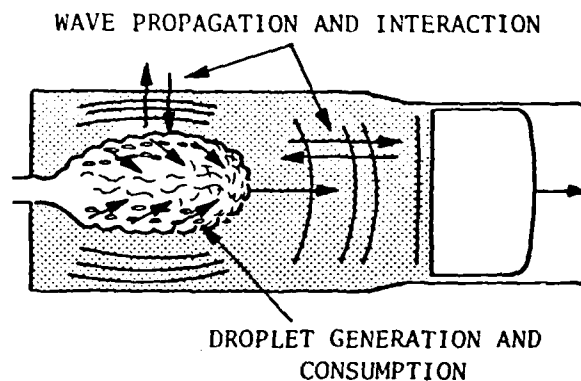
d) DEVELOPMENT OF SO-CALLED "TAYLOR" CAVITY

WAVE PROPAGATION AND INTERACTION

DROPLET GENERATION AND CONSUMPTION
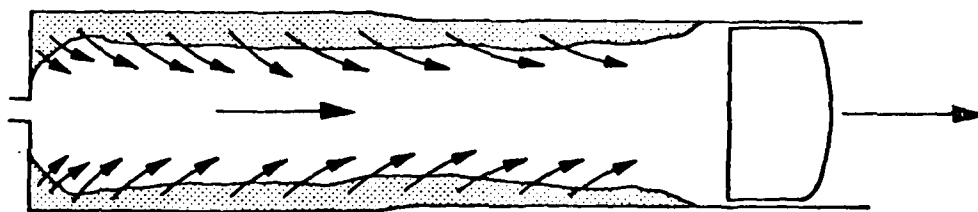
e) REGIME OF INTENSE MIXING AND COMBUSTION

Figure 1. Schematic of the Bulk Loaded LPG Firing Cycle.

4

Figure 1(c) shows ignition which involves chemical initiation, pressure build-up, jet interaction, the development of a gas bubble and the compression waves associated with the rapidly developing combustion process. As the combustion process proceeds, the pressure will tend to rise at a rate depending upon the balance between the rate of energy released due to combustion and the rate of volume increase of the gas bubble (or cavity). When the pressure at the base of the projectile is sufficiently high to overcome shot-start, the projectile will begin to accelerate which augments the rate of increase of volume.

Figure 1(d) shows the developing cavity at an intermediate stage, i.e., prior to intercepting the base of the projectile. Although asymmetries have been observed, the cavity tends to propagate down the middle of the chamber because motion in the radial direction is damped by the chamber wall. Furthermore, the cavity tip velocity is higher than the projectile velocity because its cross-section is smaller than the chamber cross-section and the relative velocity is required in order to satisfy conservation of mass. As the cavity develops in this manner, the propellant is deposited on the wall forming a slow moving layer. The relatively slow motion of the annulus primarily to its higher density and to its viscosity. A higher relative velocity develops between the propellant and the gas cavity which results in the entrainment of propellant at a rate proportional to the relative velocity (commonly referred to as Helmholz mixing). Prior to the penetration of the cavity to the base of the projectile, the relative velocity between the annulus and the cavity can be higher than at times following penetration. This is due to the higher cavity velocity relative to the projectile velocity. If the burning rate is entrainment-controlled, then once ignition and sustained combustion are achieved, two pressure plateaus can be expected. Since both the burning rate and the rate of volume increase are proportional to the velocity then constant pressure burning is possible. Thus, prior to and following cavity penetration, pressure plateaus can occur: see Figure 1(e). The duration and relative pressure levels of these plateaus depend upon the relationship between the velocity and burning surface area.

Although the problem represents a complex coupling of multiphase reacting flow phenomena, the various regimes of flow are qualitatively well defined. As a consequence, it is possible to view each discrete phase of the

5

firing cycle and then piece together a quantitative description which delineates the mechanisms responsible for many of the experimental observations.

As already cited, several models for bulk loaded LPGs have been introduced in the past in various attempts to achieve a better understanding of the interior ballistics process [1, 2, 3, 4]. However, a crucial feature common to most of these models is that they lack significant predictive capability. This characteristic can be traced to the assumptions in the model formulations which, in virtually all cases, include the constraint of either a zero or one-dimensional spatial variation [5, 6]. This constraint by itself does not preclude these types of models from providing some insight into the combustion process but rather limits them from providing information on how to control the combustion process. For example, ignition and flame propagation involve radial as well as axial transport and chemical reaction. In addition, large scale vortical structures can develop due to jetting of the ignition gases and the shear forces at the gas-liquid interface. The importance of these processes, their coupling and their relationship to geometric parameters require that a multidimensional framework be used to examine the problem in terms of a fundamental view of each of the mechanisms of potential importance to the combustion process.

SECTION 3
THEORETICAL FRAMEWORK

The observations described in the preceeding section have led to the delineation of a number of mechanisms that are important to the liquid propellant combustion process. These mechanisms include:

- Wave Dynamics
- Turbulent Transport
- Chemical Kinetics
- Multiphase Flow

The study of these mechanisms has been carried out within a framework of fundamental describing equations that include conservation of mass, momentum, energy and chemical species as well as thermal and caloric equations of state and appropriate initial and boundary conditions. These equations include descriptions of continuous liquid and gas phases and the dispersed liquid drop phases. Noting that a control volume differencing approach has been used in the numerical treatment of these equations it is convenient to express them here in integral form for a finite difference grid element which may be in motion with an arbitrary, prescribed velocity $\vec{u}$. Denoting the time-varying volume element by $V(t)$, its surface by $S(t)$ and the outward normal unit vector $\hat{n}$, the governing equations are:

$$\frac{\partial}{\partial t} \int_{V(t)} \rho_i \, dV - \int_{S(t)} \rho_i \, (\vec{U} - \vec{u}_g) \cdot \hat{n} \, dS$$

$$= - \int_{S(t)} \hat{n} \cdot \vec{J}_i \, dS + (\dot{W}_{\ell g})_i + \sum_{j=1}^{N_d} (\dot{W}_{dg})_{j,i} + (\dot{W}_g)_i \quad (i=1,N_g) \quad (1)$$

where ρ_i is the density of the ith gas species ($\rho_i = \alpha_i \rho$, where α_i is the mass fraction of the ith gas species and ρ is the total density); $\vec{U}$ is the grid velocity; $\vec{u}_g$ is the gas velocity; $\vec{J}_i$ is the ith gas phase species diffusive mass flux; $(\dot{W}_{\ell g})_i$ is the ith gas species production rate by bulk liquid consumption; $(\dot{W}_{dg})_{j,i}$ is the ith gas species production rate by j^{th} drop class consumption; $(\dot{W}_g)_i$ is the net i^{th} gas species production rate by gas phase reactions; N_g is the number of gas species and N_d is the number of drop classes.

Conservation of bulk liquid mass

$$\frac{\partial}{\partial t} \int_{V(t)} \rho_\ell \, dV - \int_{S(t)} \rho_\ell \, (\vec{U} - \vec{u}_\ell) \cdot \vec{n} \, dS$$

$$= - \int_{S(t)} \vec{n} \cdot \vec{J}_\ell \, dS - \sum_{j=1}^{N_g} (\dot{W}_{\ell g})_i - \sum_{j=1}^{N_d} (\dot{W}_c)_j \tag{2}$$

where ρ_ℓ = bulk liquid density, $\vec{u}_\ell$ is the bulk liquid velocity; $\vec{J}_\ell$ is the bulk liquid species molecular and turbulent mass transport; and $(\dot{W}_c)_j$ is the jth drop class mass production rate by atomization from the bulk liquid.

Conservation of drop mass (j^{th} drop class)

$$\frac{\partial}{\partial t} \int_{V(t)} \rho_j \, dV - \int_{S(t)} \rho_j \, (\vec{U} - \vec{u}_j) \cdot \vec{n} \, dS$$

$$= - \int_{S(t)} \vec{n} \cdot \vec{J}_j \, dS + (\dot{W}_c)_j - \sum_{i=1}^{N_g} (\dot{W}_{dg})_{j,i} \qquad (j=1, N_d) \tag{3}$$

8

where ρ_j is the jth drop species density; $\vec{u}_j$ the velocity of the jth droplet class; and $\vec{J}_j$ is the jth drop species turbulent mass transport. Partial and total mass conservation equations can be derived by various combinations of Eqs. (1)-(3).

Conservation of momentum (gas phase)

$$\frac{\partial}{\partial t} \int_{V(t)} \rho_g \vec{u}_g \, dV - \int_{S(t)} \rho_g \vec{u}_g (\vec{U} - \vec{u}_g) \cdot \vec{n} \, dS$$

$$= - \int_{V(t)} \epsilon_g \vec{\nabla} p \, dV - \int_{S(t)} \vec{\vec{\tau}}_g \cdot \vec{n} \, dS$$

$$+ \sum_{j=1}^{N_d} \left[\vec{D}_j + \sum_{i=1}^{N_g} (\dot{W}_{dg})_{j,i} \cdot \vec{u}_j \right] + \sum_{i=1}^{N_g} (\dot{W}_{\ell g})_i \cdot \vec{u}_{\ell g} \qquad (4)$$

where ρ_g is the gas density $(\rho_g = \sum_{j=1}^{N_g} \alpha_i \rho_i)$; ϵ_g is the volume fraction occupied by the gas (void fraction); $\vec{\vec{\tau}}_g$ is the gas molecular and turbulent momentum transport tensor, D_j is the drag exerted by the jth drop class on the gas and $\vec{u}_{\ell g}$ is the liquid velocity at the bulk liquid-gas interface.

Conservation of momentum (bulk liquid)

$$\frac{\partial}{\partial t} \int_{V(t)} \rho_\ell \vec{u}_\ell \, dV - \int_{S(t)} \rho_\ell \vec{u}_\ell (\vec{U} - \vec{u}_\ell) \cdot \vec{n} \, dS$$

$$= - \int_{V(t)} \epsilon_\ell \vec{\nabla} p \, dV - \int_{S(t)} \vec{\vec{\tau}}_\ell \cdot \vec{n} \, dS$$

$$- \sum_{i=1}^{N_g} (\dot{W}_{\ell g})_i \vec{u}_{\ell g} - \sum_{j=1}^{N_d} (\dot{W}_c)_j \vec{u}_{\ell d} \qquad (5)$$

9

where ϵ is the volume fraction occupied by the bulk liquid; $\vec{\tau}_\ell$ is the shear stress in the bulk liquid phase; and $\vec{u}_{\ell d}$ is the liquid velocity at the liquid-gas interface.

Conservation of drop momentum (j^{th} class)

$$\frac{\partial}{\partial t} \int_{V(t)} \rho_j \, \vec{u}_j \, dV - \int_{S(t)} \rho_j \, \vec{u}_j \, (\vec{U} - \vec{u}_j) \cdot \vec{n} \, dS$$

$$= -\int_{V(t)} \epsilon_j \vec{\nabla} p \, dV - \int_{S(t)} \vec{\vec{\tau}}_j \cdot \vec{n} \, dS - \vec{D}_j$$

$$+ \sum_{j=1}^{N_d} \dot{W}_c \, \vec{u}_{\ell d} - \sum_{i=1}^{N_g} (\dot{W}_{dg})_{j,i} \cdot \vec{u}_j \tag{6}$$

where ϵ_j is the volume fraction occupied by the jth drop class; and $\vec{\vec{\tau}}_j$ is the jth drop class turbulent momentum transport tensor.

Conservation of energy (gas phase)

$$\frac{\partial}{\partial t} \int_{V(t)} \rho_g \, e_g \, dV - \int_{S(t)} \rho_g \, e_g \, (\vec{U} - \vec{u}_g) \cdot \vec{n} \, dS$$

$$= -\int_{V(t)} \epsilon_g \, \vec{u}_g \cdot \vec{\nabla} p \, dV - \int_{S(t)} \vec{u}_g \cdot (\vec{\vec{\tau}}_g \cdot \vec{n}) \, dS$$

$$- \int_{S(t)} \sum_{i=1}^{N_g} e_i \, \vec{n} \cdot \vec{J}_i \, dS - \int_{S(t)} \vec{n} \cdot \vec{q}_g \, dS \quad.$$

(equation 7 continues on the next page)

10

$$+ \sum_{j=1}^{N_d} \left[\vec{u}_g \cdot \vec{D}_j + e_j \sum_{i=1}^{N_g} (\dot{W}_{dg})_{j,i} \right] + e_\ell \sum_{i=1}^{N_g} (\dot{W}_{\ell g})_i - q_{g\ell} - q_{gd}$$

$$(7)$$

where e_g, e_i, e_j, and e_ℓ are the specific total energies of the gas phase, i^{th} gas species, j^{th} drop class, and bulk liquid, respectively; q_g represents heat transfer by conduction within the gas phase; and $q_{g\ell}$ and q_{gd} represent interphase heat transfer between the gas phase and the bulk liquid and drops, respectively.

Conservation of energy (bulk liquid)

$$\frac{\partial}{\partial t} \int_{V(t)} \rho_\ell \, e_\ell \, dV - \int_{S(t)} \rho_\ell \, e_\ell \, (\vec{U} - \vec{u}_\ell) \cdot \vec{n} \, dS$$

$$= - \int_{V(t)} \epsilon_\ell \, \vec{u}_\ell \cdot \vec{\nabla} p \, dV - \int_{S(t)} \vec{u}_\ell \cdot (\vec{\tau}_\ell \cdot \vec{n}) \, dS$$

$$- \int_{S(t)} e_\ell \, \vec{n} \cdot \vec{J}_\ell \, dS - \int_{S(t)} \vec{n} \cdot \vec{q}_\ell \, dS$$

$$- e_\ell \left[\sum_{i=1}^{N_g} (\dot{W}_{\ell g})_i + \sum_{j=1}^{N_d} (\dot{W}_c)_j \right] + q_{g\ell}$$

$$(8)$$

where q_ℓ represents heat transfer by conduction within the bulk liquid phase.

Conservation of drop energy ($j^{\underline{th}}$ drop class)

$$\frac{\partial}{\partial t}\int_{V(t)}\rho_j\,e_j\,dV - \int_{S(t)}\rho_j\,e_j\,(\vec{U}-\vec{u}_j)\cdot\vec{n}\,dS$$

$$= -\int_{V(t)}\varepsilon_j\,\vec{u}_j\cdot\vec{\nabla}p - \int_{S(t)}\vec{u}_j\cdot(\vec{\tau}_j\cdot\vec{n})\,dS$$

$$-\int_{S(t)}e_j\,\vec{n}\cdot\vec{J}_j\,dS - \int_{S(t)}\vec{n}\cdot\vec{q}_j\,dS - \vec{u}_j\cdot\vec{D}_j$$

$$-(\vec{u}_g - \vec{u}_j)\cdot\vec{D}_j - e_j\sum_{i=1}^{N_g}(\dot{W}_{dg})_{j,i} + e_\ell\,(\dot{W}_c)_j + q_{gd} \qquad (9)$$

where q_j represents heat transfer by conduction within the jth droplet class, and we have assumed that frictional drop-gas heating goes to the drops.

The equations governing full non-equilibrium LPG dynamics are completed by defining appropriate constitutive relations for the within-phase and interphase transport of mass, energy and momentum, and by incorporating appropriate equations of state for each of the phases. It should be noted that the equations have been written in generalized vector form for compactness. When the appropriate conversion is carried out to relate these equations to an axisymmetric physical coordinate system, equations for axial, radial, and tangential mass, momentum, and energy transport are obtained. Thus, the effects of swirl which may exert a significant influence on the LPG combustion dynamics can be treated within this theoretical framework.

A large subset of Eqs. (1)-(9) is currently incorporated in the model representing gaseous, bulk liquid, and droplet phases, with the droplet phase dynamics computed under the assumption of near dynamic equilibrium and thermal equilibrium between the droplets and the surrounding gas. Because of

this assumption, the interphase transport terms representing drag effects on the droplets and gas phase and thermal energy transport between droplet and gas phase are implicit in this limit. On the other hand, this limit provides a useful baseline from which these particular non-equilibrium effects can be systematically introduced to establish their isolated effects on the combustion process.

The computational technique outlined in Ref. 3 forms the basis for the numerical solution of the governing equations. This technique utilizes a staggered grid, which may be moving to aid in establishing boundary conditions in problems with moving boundaries, and a control volume differencing approach as is reflected by the integral form in which the conservation equations have been written. In the current computer model with the near-dynamic and thermal equilibrium formulation, a quasi-Eulerian framework is used for the solution of the particle transport equations, as is appropriate when the mean motion of the particles is essentially the same as that of the gas phase. However, for the general nonequilibrium case, the use of a Lagrangian approach has been under investigation.

If dynamic equilibrium is assumed to exist, so that $\vec{u}_c = \vec{u}_d = \vec{u}$, and either thermal equilibrium ($T_c = T_d = T$) is assumed or the droplet phase temperature is specified, so that e_j is known, the equations given above can be written in terms of mixture quantities, yielding:

Conservation of mass:

$$\frac{\partial}{\partial t} \int_{V(t)} \rho dV - \int_{S(t)} \rho(\vec{U}-\vec{u}) \cdot \hat{n}dS = 0 \qquad (10)$$

Conservation of momentum:

$$\frac{\partial}{\partial t} \int_{V(t)} \rho\vec{u}dV - \int_{S(t)} \rho\vec{u}(\vec{U}-\vec{u}) \cdot \hat{n}dS + \int_{S(t)} P\hat{n}dS = \int_{S(t)} \underline{\underline{\tau}}\hat{n}dS$$

$$(11)$$

where $\underline{\underline{\tau}} = \underline{\underline{\tau}}_d + \underline{\underline{\tau}}_c$,

Conservation of energy:

$$\frac{\partial}{\partial t} \int_{V(t)} \rho e_T dV - \int_{S(t)} \rho e_T(\vec{U}-\vec{u}) \cdot \hat{n} dS + \int_{S(t)} (\hat{n}\cdot\vec{u})P dS$$

$$= \int_{S(t)} \hat{n} \cdot \vec{u}\underline{\underline{\tau}} dS + \int_{S(t)} \hat{n} \cdot (\Sigma e_j J_{jt} \Sigma e_i J_i) dS + \int_{S(t)} \hat{n} \cdot (q) dS \qquad (12)$$

Conservation of species (continuous phase):

$$\frac{\partial}{\partial t} \int_{V(t)} \alpha_i dV - \int_{S(t)} \rho F_i(\vec{U}-\vec{u}) \cdot \hat{n} dS$$

$$= \int_{S(t)} \hat{n} \cdot (J_i) dS + \int_{V(t)} [\dot{W}_i] \, dV + \dot{W}_{dg}^i - \dot{W}_c^i \qquad (13)$$

and

Conservation of species (droplet phase):

$$\frac{\partial}{\partial t} \int_{V(t)} \rho \alpha_\iota dV - \int_{S(t)} \rho \alpha_j(\vec{U}-\vec{u}) \cdot \hat{n} dS$$

$$= \int_{S(t)} \hat{n} \cdot (J_j) dS + W_c^i - W_{dg}^j \qquad (14)$$

Species production rates and droplet production rates are needed to define the appropriate mass fractions, while droplet drag and heat transfer laws must be defined to determine the effects of the presence of droplets only under full non-equilibrium conditions.

The initial investigations were carried out without explicitly considering the presence of droplets. With this further simplifying assumption, Eqs. 13 and 14 were replaced by:

$$\frac{\partial}{\partial t} \int_{V(t)} \rho F_i dV - \int_{S(t)} \rho F_i (\vec{U} - \vec{u}) \cdot \hat{n} dS$$

$$= \int_{V(t)} W_i \ dV + \int_{S(t)} \hat{n} \cdot J_i \ dS \qquad (15)$$

$$\sum_i \alpha_i = 1 \text{ and } \rho_i = \rho \alpha_i \qquad (16)$$

Any of these systems of equations, Eqs. 1 through 9, Eqs. 10 through 14, or Eqs. 10 through 12 and Eq. 15 is closed by appending thermal and caloric equations of state, a turbulence diffusivity prescription and reaction rate formulations which depend on the reactive system being considered.

Equation sets 10 through 14 and 10 through 12 and 15 have been formulated for solution using an arbitrary Lagrangian-Eulerian numerical technique. This method uses a finite-difference mesh with grid points which may move with the fluid (Lagrangian), be held fixed (Eulerian) or be moved in any other prescribed manner [8]. An implicit formulation permitting accurate solutions to be obtained for flows at all speeds is also incorporated.

To complete this set of equations, initial and boundary conditions must also be specified. The model has provisions for the selection of arbitrary initial and boundary conditions as well as general specifications of the propellant condition to allow the investigation of a variety of potentially important effects including ignition strengths, location and type; the presence of distributed ullage in various degrees as well as generalized geometries.

THE EQUATIONS OF STATE

Thermal and caloric equations of state are required to determine the local pressure and temperature. For a multi-species fluid, separate equations of state are required for each species i and may be written in functional form as follows:

$$P_i = f_i(\rho_i, T_i) \qquad \text{thermal}$$

$$e_i = g_i(c_{v_i}, T_i) \qquad \text{caloric}$$

where ρ_i, T_i, c_{v_i}, and e_i are the species density, temperature, specific heat, and specific internal energy respectively. The specific functional form for the species under consideration is of considerable interest since no single equation has yet to be demonstrated most appropriate for LPG work. Thus, in the model provisions have been made for the inclusion of several equations of state, the purpose being to provide a means of evaluating sensitivities of the LPG combustion process to the equation of state.

Currently the liquid thermal equation of state is assumed to take the form of a modified Gruneisen equation given by

$$P_\ell = c^2(\rho_\ell - \rho_0) + (\gamma_\ell - 1)\rho_\ell c_{v_\ell}(T - T_0) + P_0 \tag{17}$$

where c, ρ_ℓ, ρ_0, γ_ℓ, c_{v_ℓ}, T_0, P_0 are the liquid sound speed, density, ambient density, ratio of specific heats, specific heat at constant volume, ambient temperature and ambient pressure, respectively. This equation is advantageous from the standpoint that it has a simple functional relationship for the pressure and includes the effects of compressibility. Other equations of state for the bulk liquid have been developed through semi-empirical approaches for the application to high pressure systems and warrant consideration in the future. For example, Burnett [4] suggests three equations of state applicable to the regime of interest here.

For the gas phase, thermal equations of state range from the ideal gas law to virial representations obtained from extrapolations of known gas behavior in temperature and pressure ranges applicable to the LPG problem. Currently the model includes provisions for defining the gas phase pressure in terms of the ideal gas law

$$P_g = (\gamma_g - 1)\rho_g c_{v_g} T \tag{18}$$

or in terms of a covolume relationship

$$P_g = \frac{(\gamma_g - 1)\rho_g c_{v_g}}{(1 - \beta \rho_g)} \tag{19}$$

where β is the covolume parameter.

16

The ideal gas law is known to be inaccurate for dense gases leaving the covolume relationship which takes into account the excluded volume of the compacted molecules as the better representation for the gas phase. However, this latter approach too has its drawbacks, the most serious of which is the paucity of data at higher temperatures required to establish the value of the covolume parameter. In addition to the two representations above, virial relationships for the dense gas pressure are also being considered. Recent studies [9] have demonstrated, for example, that for aqueous mixtures of the type considered here it is important to include the effects of the dipole water molecule in the determination of the gas pressure and this may be accomplished if virial relationships, which have been defined for the temperature and pressure ranges of interest here, are included.

The application of any of these equations of state is straightforward for volumes containing either liquid or gas. However, for cell volumes which contain both liquid and gas, additional relationships must be included to determine the pressure. If phase equilibrium is assumed then species pressure equilibrium can be imposed

$$P = P_\ell = P_g \tag{20}$$

and under the further stipulation that mass and volume must be conserved, an iterative technique is used in which the species specific volumes are adjusted in such a manner as to conserve mass and volume until pressure equality is obtained.

Liquid-Gas Interactions

The development of the Taylor cavity creates a liquid-gas interface that is subjected to destabilizing accelerations and shear stresses. The transition from an organized motion including large scale coherent vortical structures to random, or turbulent, motion can be traced to the growth of disturbances on the interface. However, early attempts to apply linear instability theory to the LPG combustion process [1] proved to be inadequate in explaining the high burning rates observed in LPG firings. Comer demonstrated that the linearity assumption is violated long in advance of the development of the surface area required to account for the high burning rates. In fact, it was shown that non-linear effects become important in times approaching one order of magnitude less than typical burn times, which range from approximately 1

17

to 5 msec. The results of these studies suggest that fully developed turbulent mixing is an appropriate assumption for the bulk of the LPG firing cycle. Liquid propellant gun researchers, most notably Comer, adopted an approach based upon an extension of the Helmholtz instability mechanism applicable to the non-linear regime [10-12]. The latter studies involved the development of a semi-empirical relationship for the rate of entrainment of liquid into a gas flowing parallel to the contact surface; viz.,

$$\dot{r} = \gamma_W \Delta u \tag{21}$$

where $\dot{r}$ is the "linear regression rate" of the liquid surface, γ_W is the so-called Helmholtz "wiping" coefficient, and Δu is the relative velocity between the liquid and gas.

The problem with this approach is that the values of γ_W that are derived using Eq. 21 in the interpretation of available LPG firing data are quite small in comparison with those reported for liquid/gas mixing. In this regard it is important to note that Comer [1] required the use of the smallest reported value of γ_W, 0.04, in order to explain his data. Comer's small value of γ_W can, however, be explained in terms of more classical gas-gas turbulent mixing phenomenology [2]. That work has shown that

$$0.016 < \gamma_W < 0.032. \tag{22}$$

Thus, what was a minimum value of γ_W based on liquid entrainment turns out to be of the same order of magnitude as the maximum value based upon classical concepts of gas-gas turbulent mixing. Furthermore, this result explains the "small" γ_W = 0.04 required by Comer in the process of fitting his data. Of additional significance here is the consistency of this result with the fact that the operating conditions in a typical LPG will be above the critical state over much of the burn time. Thus, gas-gas mixing would be expected to apply under such conditions.

Turbulence modeling approaches range from the definition of a spatially and temporally constant eddy viscosity through attempts at direct solution of the governing equations for the turbulence components that represent the turbulent shear stress. Of this range of approaches, the most widely used

18

are the algebraic models which relate the eddy viscosity to local mean flow properties and the transport models which relate the turbulent shear stress (or eddy viscosity) to some transportable turbulence characteristic, such as the turbulent kinetic energy. Both of these approaches can yield accurate results in turbulent, reacting flowfields [13] but the most general approach (i.e., most widely applicable without changes in modeling assumptions) involves the use of turbulent kinetic energy methods.

Because of the dearth of data on transient flows and the need to establish sensitivities, a hierarchy of analyses and assumptions was employed in the current studies. To approximate the effects of turbulence on mixing rate, a constant eddy diffusivity was employed, while to establish the importance of model assumptions a simple locally flow-dependent turbulence model was used. Results, discussed in detail later, show both the importance of turbulence and the remarkable effect that accounting for the locally flow-dependent nature of the turbulence can have on the cavity shape. These results clearly support the consideration of the more general multi-equation turbulent kinetic energy methods [13] for this problem. For example, the two-equation turbulence model [14] has been utilized in a wide variety of applications, including transient and multiphase flows [15]. In this approach, the turbulent momentum transport tensor is modeled under a gradient transport assumption: *the turbulent shear stress is given by the product of an eddy viscosity coefficient and the appropriate velocity gradient*, e.g.,

$$\tau_{xy} = \mu_T \frac{\partial u}{\partial y} \tag{23}$$

and so on. The viscosity coefficient μ_T is obtained from the solution of two additional transport equations, one for the turbulent kinetic energy k (which represents the energy contained in the fluctuating velocity components) and a second for the turbulence dissipation rate ϵ. Then

$$\mu_T = C_\mu \, \rho \, k^2/\epsilon \tag{24}$$

where C_μ is a constant. Note that as expressed by Eq. (24), μ_T is isotropic, i.e., attains a single value which applies to all components of the turbulent shear stress.

Since the units μ_T are mass/length x time, and a single value of μ_T is obtained for each velue of k^2/ε, Eq. (24) implies that there is a single average length scale that characterizes the turbulence at each point in the flowfield. (Note that this does not imply that one average length scale characterizes the entire flowfield, however; both k and ε vary with space and time.) The two-equation model is thus a special case of a more general set of multiple length scale models [16]. These models have been investigated with respect to their predictions of a variety of flows [17]. Because of the strong effect of length scale on diffusion time, multiple-scale models are potentially valuable for application to the modeling of chemically reacting flows. In reacting flows scales appropriate to the chemical reaction process can, using the multiple length scale approach, be defined and tracked in conjunction with scales appropriate to the turbulent mixing process.

Both the two-equation and multiple length scale models rest on the eddy viscosity hypothesis embodies in Eq. (23), i.e., gradient diffusion. A more fundamental approach is to directly predict the turbulent shear stress through use of the Reynolds stress transport equations for each of the stress components. While this approach avoids both the eddy viscosity assumption and the isotropic stress assumption, each of the Reynolds stress equations contains terms which must still be modeled through the judicious use of physical assumptions, and the complete set of equations form a complex system (involving five transport equations for a two-dimensional flow).

A simple version of the Reynolds stress modeling approach which still retains most of the positive features of the technique is the algebraic Reynolds stress model proposed by Rodi [18]. In this approach the Reynolds stress equations are reduced, using simplifying assumptions, to three algebraic relations to be used in conjunction with differential transport equations for k and ε. In a variety of applications this approach has been shown to provide a useful increase in generality relative to the two-equation model [19]. The algebraic stress model is, however, computationally more difficult to handle than the basic two-equation approach.

Currently, the hierarchy contained in the computerized LPG code includes the constant effective eddy diffusivity, a locally flow-dependent eddy diffusion, and the two-equation formulation. The first two of these models

20

have been used successfully to predict trends and to delineate the sensitivities of the LPG combustion process to turbulence.

While potentially important improvements in the description and accuracy of turbulence modeling have been cited the critically important heat release process must also be accurately described in order to properly separate physical and chemical effects.

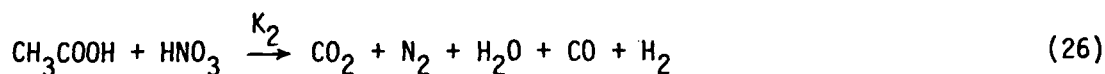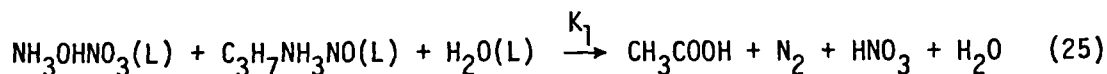## Chemistry and Chemical Kinetics

Observations ranging from fizz burning (partial oxidation) to excessively rapid burning following an ignition delay period indicate that the chemistry and chemical kinetics of the LPG process play crucial roles in the early phase of the combustion process. The major transitions appear to involve decomposition followed by the generation of the final products of combustion through a series of exothermic reactions. The initial decomposition of monopropellants that have been considered for LPG applications is thought to be by dissociative vaporization. This has been likened to a "manufacturing" process wherein lighter molecular weight compounds are formed and enter into the reaction acting as the fuel and oxidizer during the more exothermic phase of combustion. This type of process appears to be relevant to the description of the combustion of aqueous solutions of liquid hydroxylammonium nitrate (HAN), and isopropylammonium nitrate (IPAN). The generic composition of this class of propellant is given in Table 1.

TABLE I. HAN/IPAN PROPELLANT

NAME	CHEMICAL FORMULA	FORMULA MASS
Hydroxylammonium nitrate	NH_3OHNO_3 (L)	96.048
Isopropylamine nitrate	$C_3H_7NH_3NO_3$ (L)	122.129
Water	H_2O (L)	18.016

Klein of BRL has made a broad study of many of the features of the combustion of this propellant. No quantitative kinetics data were obtained, but the following observations have been made [20].

The first reaction in the ignition sequence of LP is the decomposition of HAN, producing N_2, N_2O, NO, NO_2 and HNO_3. Most of the HAN reacts before the fuel begins reacting, and it may therefore be assumed that the fuel reacts not with HAN but rather with its decomposition products. As the reaction sequence continues and the fuel becomes involved, acetic acid appears as a product. At this point, no luminosity is evident, and the rate of gas evolution has remained modest. As the concentration of the intermediates continues to accumulate, a threshold concentration is attained at which time a vigorous reaction takes place, rapidly producing gases and emitting light. Analysis of the products after the vigorous reaction involving light emission show that only N_2, CO_2 and H_2O exist. These observations suggest that two overall reaction steps are critical to the combustion process. The first reaction is the decomposition of the HAN and IPAN to form acetic acid and nitric acid, the fuel and oxidizer, respectively, for the second combustion reaction. No partially oxidized intermediates, including nitrogen species like NO and NO_2 are made by either of these reactions. The first reaction represents the "fizz-burn" since it is not strongly exothermic, and the second reaction represents the primary combustion step. Reaction equations can be postulated for these two steps in the following skeletal form.
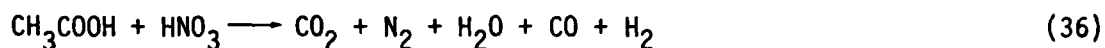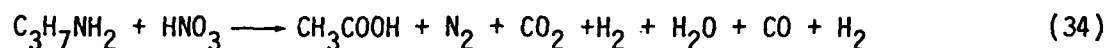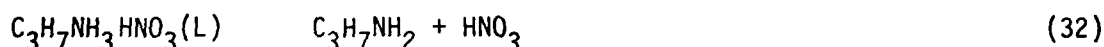
$$NH_3OHNO_3(L) + C_3H_7NH_3NO(L) + H_2O(L) \xrightarrow{K_1} CH_3COOH + N_2 + HNO_3 + H_2O \quad (25)$$

$$CH_3COOH + HNO_3 \xrightarrow{K_2} CO_2 + N_2 + H_2O + CO + H_2 \quad (26)$$

The reaction rates are represented as:

$$-\frac{dC_{IPAN}}{dt} = K_1 \, C_{HAN} \, C_{IPAN} \quad (27)$$

$$-\frac{dC_{CH_3COOH}}{dt} = K_2 \, C_{CH_3COOH} C_{HNO_3} \quad (28)$$

$$\text{where } K_i = A_i \, T^{\beta i} \, e^{-\frac{E_i}{RT}} \quad (29)$$

A further delineation of intermediate reactions and species is possible in which hydroxyl amine and isopropyl amine are the major intermediate decomposition products. The hydroxyl amine in turn decomposes, while the isopropyl amine is oxidized by the nitric acid present in the system to form acetic acid. Hydrogen is also oxidized by the nitric acid. The three decomposition reactions and the isopropylamine oxidation would account for the fizz-burn, and the acetic acid and hydrogen oxidation would represent the major exothermic combustion reactions. Since both the very unstable hydroxamine and very stable acetic acid are present in this system, a wide range of combustion/pressure interactions could be represented by this reaction mechanism. For example, the accumulation of NH_2OH followed by its rapid decomposition could produce pressure spikes like those observed in closed chamber experiments. The model resulting from these considerations is stated in skeletal form as follows.

$$NH_3OHNO_3(L) \longrightarrow NH_2OH + HNO_3 \tag{30}$$

$$NH_2OH \longrightarrow N_2 + H_2O + H_2 \tag{31}$$

$$C_3H_7NH_3HNO_3(L) \qquad C_3H_7NH_2 + HNO_3 \tag{32}$$

$$H_2O(L) \longrightarrow H_2O \tag{33}$$

$$C_3H_7NH_2 + HNO_3 \longrightarrow CH_3COOH + N_2 + CO_2 + H_2 + H_2O + CO + H_2 \tag{34}$$

$$H_2 + HNO_3 \longrightarrow H_2O + N_2 \tag{35}$$

$$CH_3COOH + HNO_3 \longrightarrow CO_2 + N_2 + H_2O + CO + H_2 \tag{36}$$

Species like CO, NO, N_2O, NO, NO_2 and pure oxygen, as well as OH, O and H can be added to this system by incorporating well established elementary reactions to completion, involving steps including the wet-CO mechanism.

In a preliminary analysis of the combustion process, the application of global kinetics was examined assuming that the chemical process is governed by a single rate-limiting step (see Table III). While this assumption is clearly an oversimplification, the results show that a sensitive balance can exist between mixing due to turbulence and the rate of reaction and that quenching can occur.

Of course, the multistep mechanism is fundamental to the study of the buildup of intermediates with the attendant violent reaction toward completion. In this case the coupling to the fluid mechanics through turbulence and wave dynamics is critical to the understanding and control of the combustion process.

Preliminary Model Assessment

The cases selected for analysis were chosen to demonstrate the utility of the current model in developing an understanding of the LPG combustion process. In this regard legitimate concerns range from numerical inaccuracies and efficiency to the potential for compensating effects that can be introduced through the assumptions made in characterizing the physical and chemical processes. Thus, a spectrum of model applications was selected ranging from a comparison with a known analytic solution, the Lagrange problem, to several examples involving LP configurations including a direct comparison with firing data. Sensitivities to numerical grid assumptions and assumptions made for turbulence and kinetic parameters are included in these preliminary studies.

The Lagrange ballistic problem presents an ideal vehicle for initially investigating the reasonableness of the assumptions made in developing the governing set of equations as well as the numerical techniques employed in their solution. The problem is one in which transient phenomena including wave propagation and wave-boundary interactions are considered. Further, the solution regime encompasses high speed flow as well as boundary motion (simulating the moving projectile) providing a test of the numerical scheme in the context of a gun environment.

The Lagrange ballistic problem consists of a projectile fitted in a perfectly smooth cylindrical chamber closed at one end. The projectile is held fixed while an inert, hot gas at high pressure is introduced at the breech end. The gas is assumed to behave inviscidly and the problem reduces to the one-dimensional expansion of the contained gas as the projectile is propelled down the gun barrel. The process is governed by rarefaction wave propagation and the waves generated can traverse the distance between the breech and the projectile several times depending on the length of the barrel considered.

If a constant covolume is imposed and it is further assumed that the expansion is isentropic, an analytic solution for the flowfield and projectile motion is possible. Love and Pidduck [21] developed such an analytic solution

and applied it to a 150 mm Lagrange gun. Their results[†] for a 150 mm gun were compared with numerical solutions using the current LPG model. Initialization parameters for this simulation are shown in Table II. Boundary conditions along the chamber wall, breech end and projectile base were assumed to be free slip, adiabatic with no mass transport normal to the boundaries.

Three simulations were run to 5 msec starting with the same initial and boundary conditions but differing in the solution technique employed. The first simulation was fully explicit with time steps limited by the Courant condition ($\Delta t \cong 10^{-2}$ msec). The second and third simulations were partially implicit which removes the acoustic wave propagation constraint (Courant condition) and allows time steps to be chosen greater than a Courant number of unity. Utilizing the ICE [22] option, the second simulation was run with a time step consistent with a Courant number of 2, while the third simulation was run at a Courant number of 4.

Figures 2 through 4 display the simulated results with Figures 2(a), 2(b) and 3(a) incorporating the analytic Love and Pidduck solution for comparison. Excellent agreement between the simulated and analytic solutions is apparent in these figures. The high accuracy of the numerical solutions indicates the correctness of the basic numerical approach utilized in the LPG model for the conditions specified in this problem.

Figure 2(a) shows the breech end pressure trace as a function of time. A discontinuity in the pressure slope at approximately 1 msec is caused by the reflection of the rarefaction wave at the breech end. The analytic solution also indicates a wave reflection at this time implying that the correct wave speed is being predicted in the numerical solution. In Figure 2(b), the reflected rarefaction wave reaches the projectile base at 0.21 msec as denoted by the knee in the pressure curves at this time. Some slight pressure "smearing" is shown for the implicit cases pointing out some small loss of wave resolution at the larger time steps. The associated projectile speed is shown in Figure 3(a). A smooth rise in projectile velocity is noted with excellent agreement between the analytic and numerical solutions. This figure also shows that large velocities are developed (61 cm/msec at 5 msec) within the propelling gas. The presence of high flow velocities can induce

---

[†]The authors wish to acknowledge the efforts of James Schmidt of the Ballistics Research Laboratory who consolidated the background material on the Lagrange ballistic problem.

25

TABLE II.
GEOMETRY AND GAS PROPERTIES FOR THE
150 mm LAGRANGE GUN SIMULATIONS

CHAMBER GEOMETRY

L = 1698 cm   Chamber Length

R = 7.5 cm   Chamber Radius

PROJECTILE SPECIFICATION

M_p = 5 x 10^4 g   Projectile Mass

INITIAL FLUID CONDITIONS

P_0 = 621.09 MPa   Initial Pressure

T_0 = 2666.8°K   Initial Temperature

ρ_0 = 0.400365 g/cm³   Initial Density

EQUATION OF STATE PARAMETERS

$$P = \frac{(\gamma-1)\rho c_v T}{(1-\beta\rho)}$$

γ = 1.222   Ratio of Specific Heats

c_v = 1.53605 joules/gm-°K   Specific Heat

β = 1.0 cm³/g   Covolume

BOUNDARY CONDITIONS

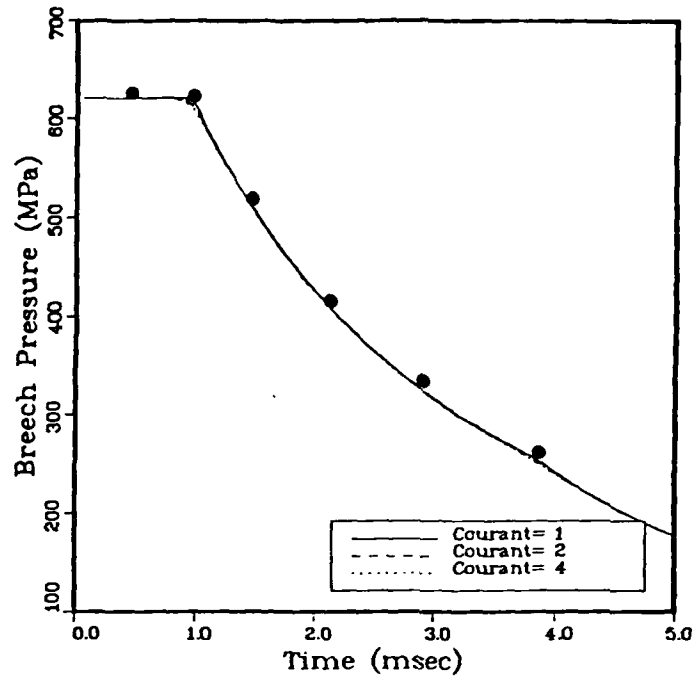|		
$\partial v/\partial r = 0$; $u = 0$	At Chamber Wall	Free Slip
$\partial u/\partial z = 0$; $v = 0$	At Breech End	Free Slip
$\partial u/\partial z = 0$; $v = v_{proj}$	At Projectile Base	Free Slip, Moving Boundary
$\partial T/\partial r = 0$; $\partial F/\partial r = 0$	At Chamber Wall	Nonporous, Adiabatic Boundary
$\partial T/\partial z = 0$; $\partial F/\partial z = 0$	At Breech End and Projectile Base	

Figure 2(a).   Breech End Pressure Trace for the
Lagrange Gun Simulations
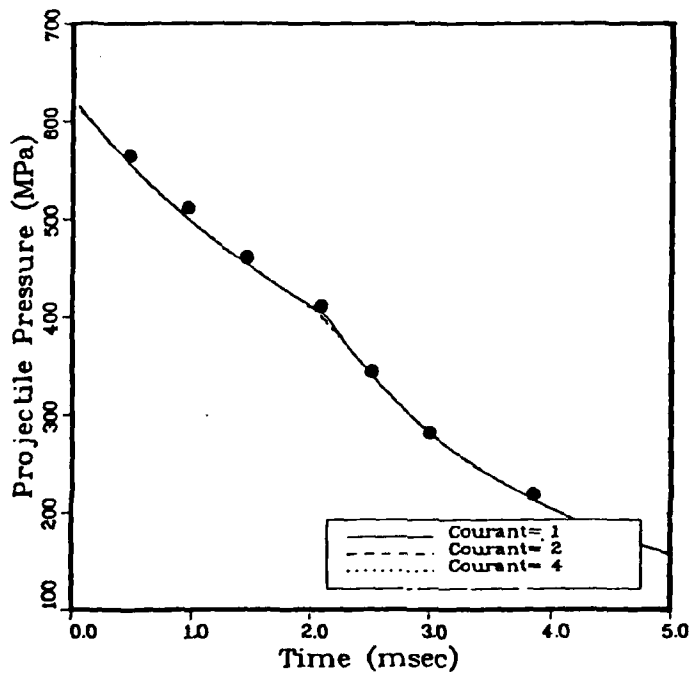(analytic solution is represented
by solid circles).

Figure 2(b).   Projectile Base Pressure Trace for
the Lagrange Gun Simulations
(analytic solution is represented
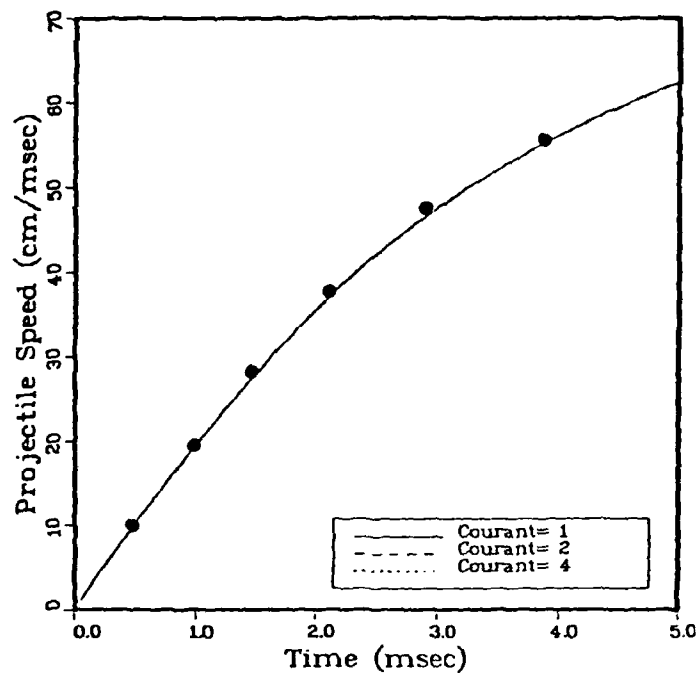by solid circles).

27

Figure 3(a).   Projectile Speed Trace for the
Lagrange Gun Simulations
(analytic solution is represented
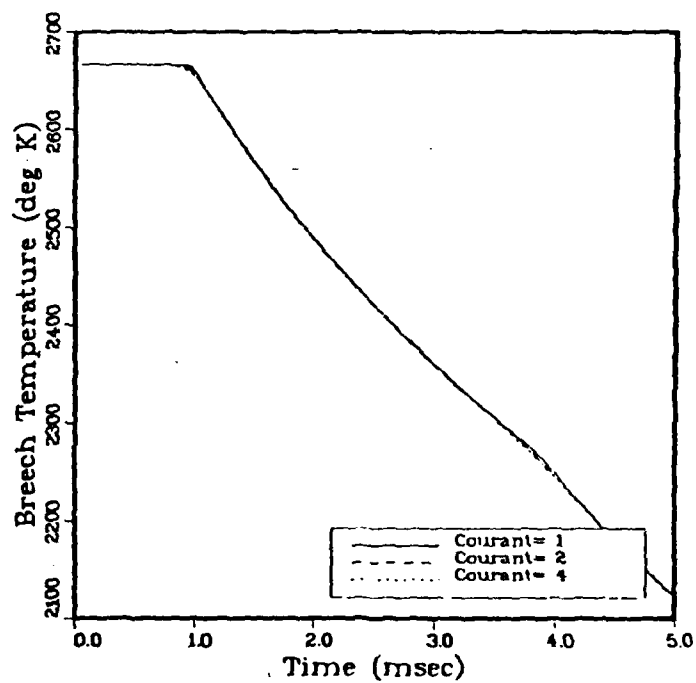by solid circles).

Figure 3(b).   Breech End Temperature-Time
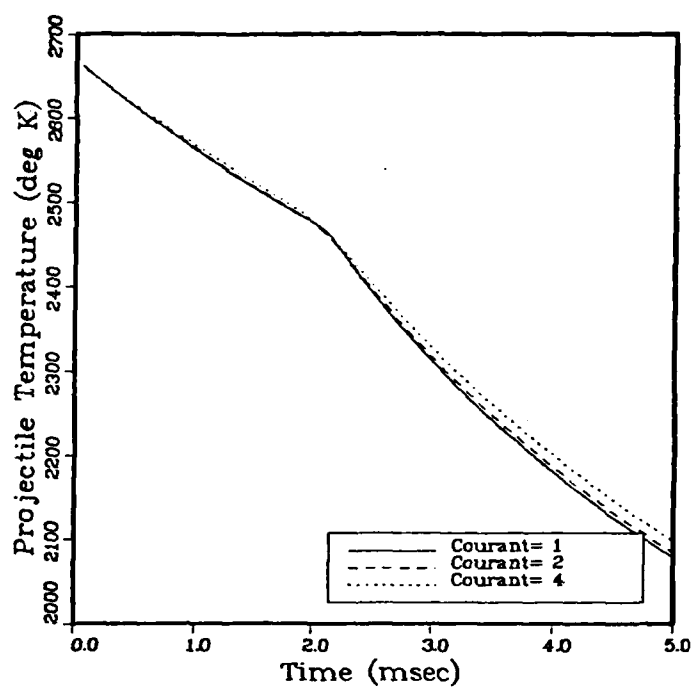Profiles for the Lagrange Gun
Simulations.

28

Figure 4. Projectile Base Temperature-Time
Profiles for the Lagrange Gun
Simulations.

large numerical diffusion effects in first order solutions like that used here (donor cell). However, the excellent agreement attained between the analytic and numerical solutions points out that numerical diffusion does not play an important role in the simulated results.
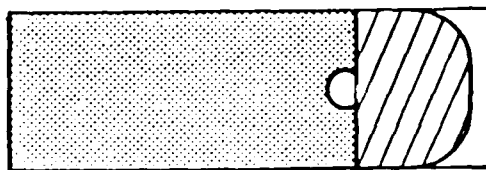
Figures 3(b) and 4 display breech end and projectile base temperature-time profiles. As noted in these figures, the adiabatic expansion of the propelling gas has decreased the chamber temperature $500^\circ K$ by 5 msec. Of interest in Figure 4 is the small discrepancy between the implicit and explicit situations (which, however, are still in good agreement). This discrepancy is due to small errors in the calculation of the velocity field which accumulate with time in the implicit solutions. While these errors are not significant here, these results do point out the need for caution when interpreting solution results obtained using time steps larger than accuracy requirements dictate (see discussion on implicitization below).

The Lagrange gun simulation was felt to be an important first step in the verification of the LPG model. The excellent agreement attained in these solutions indicates the correctness of the basic approach and the accuracy of the solution technique employed. These results are however, not sufficient to conclude that the model is accurate in the context of the LPG environment. Because the LPG involves highly transient, two-dimensional, reacting turbulent flow with strongly coupled chemical kinetics, prediction of flame propagation and the subsequent flowfield development in the LPG requires not only physically realistic model descriptions but also places more exacting requirements on the numerical aspects of the solution procedure than are demanded by the 1D Lagrange problem. Descriptions of the chemistry and turbulence submodels in the previous section include both those currently employed in the LPG code as well as future refinements slated for incorporation into the model. Studies of the physical and chemical submodels and the numerical simulation have been an ongoing feature of the current program.
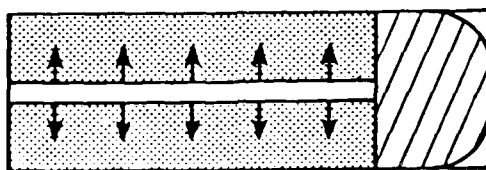
In order to establish the specific requirements for experimental data and for further theoretical model developments, a variety of LPG configurations are under investigation, Figure 5. Figure 5(a) illustrates a breech end ignition by a prechamber source and serves as the baseline calculation
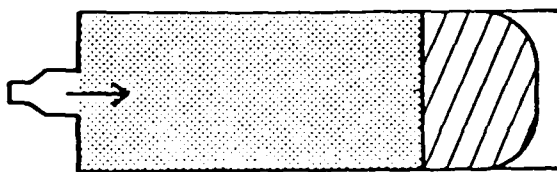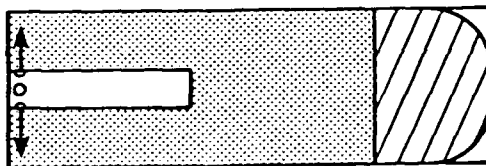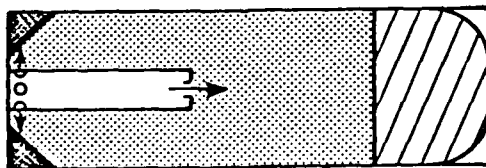
a) PRECHAMBER IGNITION   b) PROJECTILE BASE IGNITION

c) AXIAL LINE IGNITION

d) BAYONET IGNITER

e) ALTERNATE BREECH END CONFIGURATION

Figure 5.   Generic Ignition and Main Chamber Configurations

described below. Figure 5(b) displays an idealized projectile base ignition by a source placed adjacent to the projectile base. An analysis of the configuration has been carried out as a parametric study.

An actual BRL test firing was chosen as the initial test of the model's full capabilities in the context of an LPG environment. The particular test selected corresponds to the generic description in Figure 1(a) and was made in part on the basis that a previous numerical solution was available to augment and facilitate model comparisons [23].

Initializing data for this simulation may be found in Table III (baseline case). Preliminary studies showed that zones on the order of a millimeter on a side provided adequate resolution. The finite-difference grid is shown in Figure 6. The gun design includes a prechamber igniter which communicates with the main chamber through an orifice of radius 0.4 cm. This igniter was modeled as an inflow of hot gases, by imposing a flux of mass, momentum and energy for a finite time at the start of the firing cycle. The projectile is held fixed until the pressure along its base exceeds 20 MPa, simulating shot start conditions. Thereafter it is allowed to move in response to the integrated pressure impulse at its base, reduced by a friction velocity simulating engraving and frictional forces within the gun barrel. Although imposing some form of friction velocity is consistent with comparison to actual gun firing data, care must be taken so as not to mask important physical phenomena associated with the initial projectile motion. For example, the question of cavitation has been raised, and one-dimensional simulations [5] show that the possibility of cavitation does exist. If a cavitation bubble occurs at the base of the projectile, then rapid recompression of the vapor can result in high temperatures, with a consequent potential for front-end ignition. In the test cases described below, the friction velocity imposed was of sufficient magnitude so as to suppress the tendency to cavitate. This was intentional for the preliminary investigations; cavitation effects will be considered in subsequent investigations.

Figure 7 displays the resultant pressure-time trace for the baseline simulation. Included in this figure are additional curves representing an earlier LASL calculation and the results from the associated BRL test firing [23]. Good agreement between the three curves is apparent, although some

32

TABLE III
GEOMETRY AND FLUID PROPERTIES
FOR THE LPG SIMULATIONS

CHAMBER GEOMETRY

$L = 10$ cm   Chamber Length

$R = 2$ cm   Chamber Radius

ZONING

Baseline	Variable Viscosity	Projectile Base Ignition
$\Delta r = 0.1$ cm	$\Delta r = 0.1$ cm	$\Delta r = 0.1$ cm
$\Delta z_j = 0.1$ cm	$\Delta z_j = 0.1$ cm	$\Delta z_j = 0.1$ cm
from z = 0-0.5 cm	from z = 0-0.5 cm	from z = 9.5-10 cm
$\Delta z_j = \Delta z_1(1.33)^{j-5}$	$\Delta z_j = \Delta z_1(1.33)^{j-5}$	$\Delta z_1 = 1.21524$
		$\Delta z_j = \Delta z_1(0.8826)^{j-1}$

PROJECTILE SPECIFICATION

$M_p = 500$ g   Projectile Mass

$C/M = 0.7$ Charge-to-Mass Ratio

$P_s = 20$ MPa   Shot Start Pressure

INITIAL FLUID CONDITIONS

$P_0 = 0.1$ MPa   Initial Liquid Pressure

$T_0 = 300^{\circ}$K   Initial Liquid Temperature

$\rho_0 = 1.39$ g/cm^3 Initial Liquid Density

33

TABLE III (Continued)
GEOMETRY AND FLUID PROPERTIES
FOR THE LPG SIMULATIONS

EQUATION OF STATE PARAMETERS

$$P_\ell = c^2(\rho_\ell - \rho_0) + (\gamma_\ell - 1)\rho_\ell c_{v_\ell}(T - T_0) + P_0$$

$$P_g = (\gamma_g - 1)\rho_g c_{v_g} T$$

c	=	204.21 cm/msec	Liquid Sound Speed
γ_ℓ	=	1.5	Liquid Gamma
γ_g	=	1.195	Gas Gamma
c_{v_ℓ}	=	2.3860 j/g-$^\circ$K	Liquid Specific Heat
c_{v_g}	=	1.6744 j/g-$^\circ$K	Gas Specific Heat

KINETIC PARAMETERS

$$K = c_f(P/P_0)^{n_f}\phi(T)$$

c_f	=	0.00170 g/cm^3-msec	Pre-exponential Coefficient
n_f	=	1.25	Exponent

$$\phi(T) = \begin{cases} 0 & T \leq 500^\circ K \\ \dfrac{T-500}{1000} & 500 < T < 1500^\circ K \quad \text{Linear Temperature Dependence} \\ 1 & 1500^\circ K < T \end{cases}$$

TURBULENCE SPECIFICATION

Baseline	Variable Viscosity	Projectile Base Ignition
$\kappa_T = 1.0$ cm^2/msec	$\kappa_T = f(\lvert \bar{v} \rvert)$	$\kappa_T = 1.0$ cm^2/msec
	$0.1 \ \kappa_T \leq 1.0$ cm^2/msec	

34

TABLE III (Continued)
GEOMETRY AND FLUID PROPERTIES
FOR THE LPG SIMULATIONS

IGNITION PARAMETERS

Baseline	Variable Viscosity	Projectile Base Ignition
Prechamber Igniter	Prechamber Igniter	Source Deposition
Vent of Radius 0.4 cm	Vent of Radius 0.4 cm	Deposition in Last Row of Cells Within a Radius of 0.4 cm
$\rho_I = 0.1 \text{ g/cm}^3$	$\rho_I = 0.1 \text{ g/cm}^3$	$\dot{Q} = 3.01 \times 10^7 \, t(0.2-t)$ j/g-msec
$T_I = 2400^\circ K$	$T_I = 2400^\circ K$	$0 \leq t \leq 0.2$ msec
$|\overline{v}_I| = 2000 \, t(0.2-t)$ cm/msec	$|\overline{v}_I| = 2000 \, t(0.2-t)$ cm/msec	
$0 \leq t \leq 0.2$ msec	$0 \leq t \leq 0.2$ msec	

BOUNDARY CONDITIONS

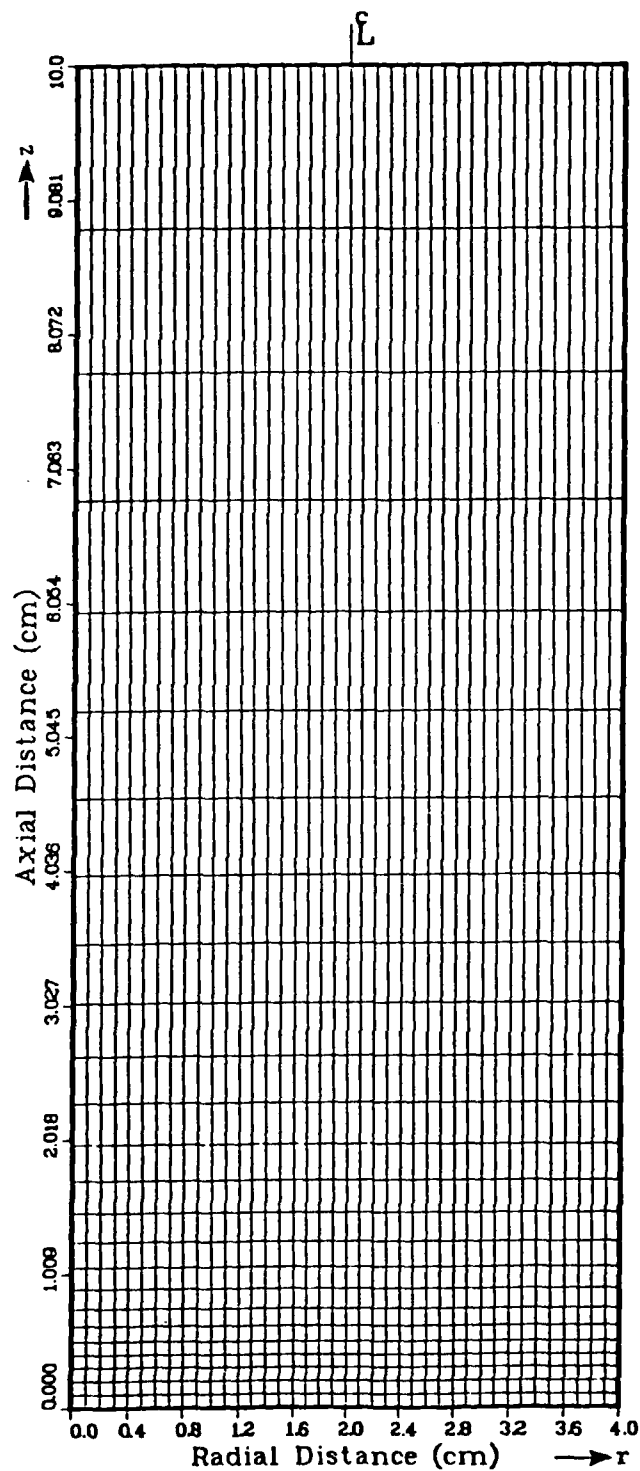|	
$u = 0, \, v = 0$	No-slip Condition at Boundaries (Except Projectile Base)
$u = 0, \, v = v_{proj}$	No-slip Moving Boundary at Projectile Base
$\frac{\partial T}{\partial r} = 0; \quad \frac{\partial F_i}{\partial r} = 0$	At Chamber Wall
$\frac{\partial T}{\partial z} = 0; \quad \frac{\partial F_i}{\partial z} = 0$	At Breech End and Projectile Base

Nonporous, Adiabatic Boundary

Figure 6. Finite-Difference Grid of the Main Chamber for the Baseline and Variable Eddy Viscosity Simulations.
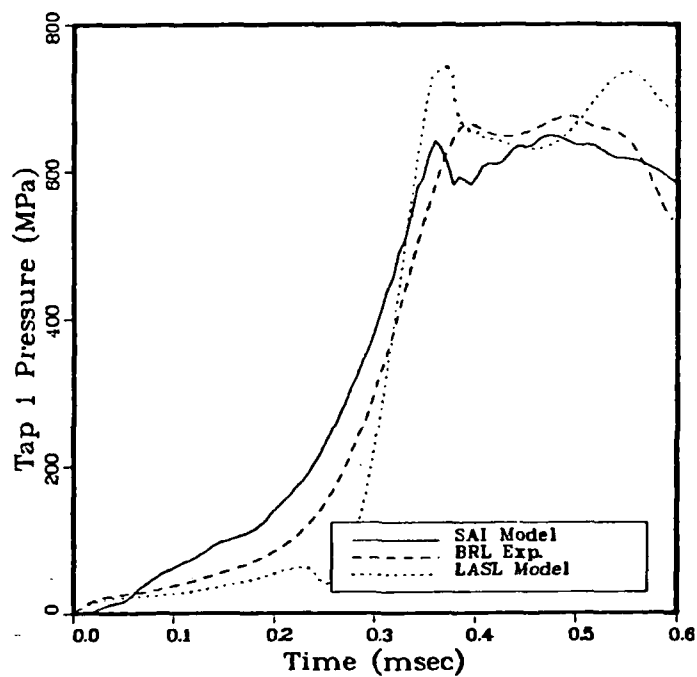
Figure 7. Pressure-Time Histories for the
Baseline Simulation at Tap 1
(3.2 cm from the breech end).

37

minor differences are noted, for example, in the position in time of the first pressure peak. However, the general structures of the curves are similar, and the pressure magnitudes fall closely together for all three curves. For purposes of discussion, the pressure-time trace may be divided into three phases. The first phase, 0-0.2 msec, will be referred to as the ignition phase and in the calculations is dominated by the structure of the ignition model. Variations between the two numerical simulations in this region are attributable to differences in the initializing assumptions. For example, differences in zoning exist between the two models. The LASL simulation employed constant zoning with spatial increments of 0.2 cm in the radial and 0.4 cm in the axial direction, while the present model utilizes a variable grid, initially 0.1 cm and expanding in the axial direction (Figure 6). Sensitivity studies performed with the current LPG model showed that this zoning was too coarse for accurate resolution of the early time behavior.

At the end of the first phase of the firing cycle sufficient energy has been deposited in the liquid propellant to raise its temperature and pressure well above the combustion threshold, and a well-defined flame front forms and moves out rapidly into the liquid. The consumption of the liquid propellant is reflected in the rapid pressure rise during the second phase, 0.2 - 0.33 msec. This second phase encompasses flame propagation not only axially down the chamber but radially out to the chamber wall. The impingement of the flame on the wall coincides with the first sharp peak in pressure (0.33 msec). The correlation of this first peak in pressure with wall flame contact is one possible explanation of the peak also noted in the test firing. The third phase, 0.33 - 0.6 msec, encompasses the time of flame propagation down the combustion chamber until burnout is achieved. Analysis of the flame interface (as is discussed below, for example see Figure 9(b)) during this period indicates that the flame front, which is initially highly curved, becomes more and more planar as the flame front moves down the chamber. This lack of curvature in the flame front is shown later to be due at least in part to the sepcification of a constant eddy diffusivity and may additionally be influenced by the coarser zoning employed near the projectile base.

As noted in Figure 7, good agreement between the simulated and experimental results has been achieved. However, while it is important to accurately predict pressure-time traces, the replication of these experimental test data
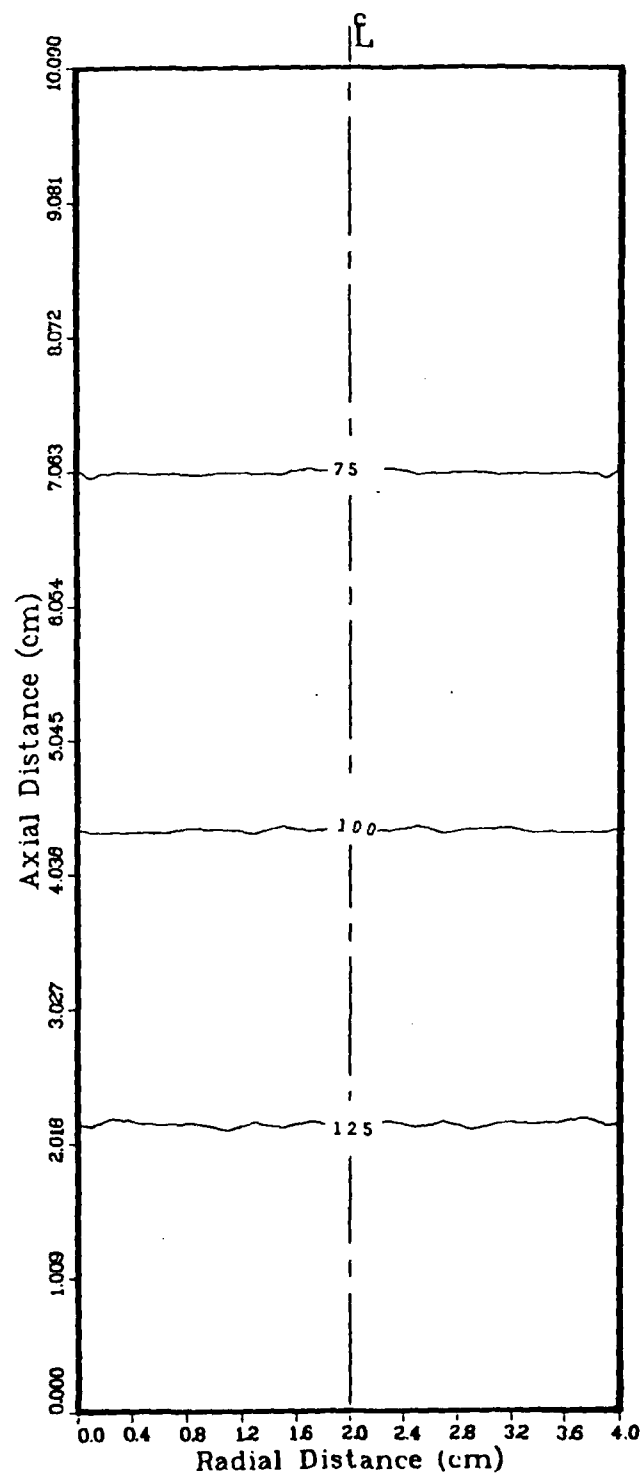
Figure 8(a). Pressure Distribution (MPa) for the
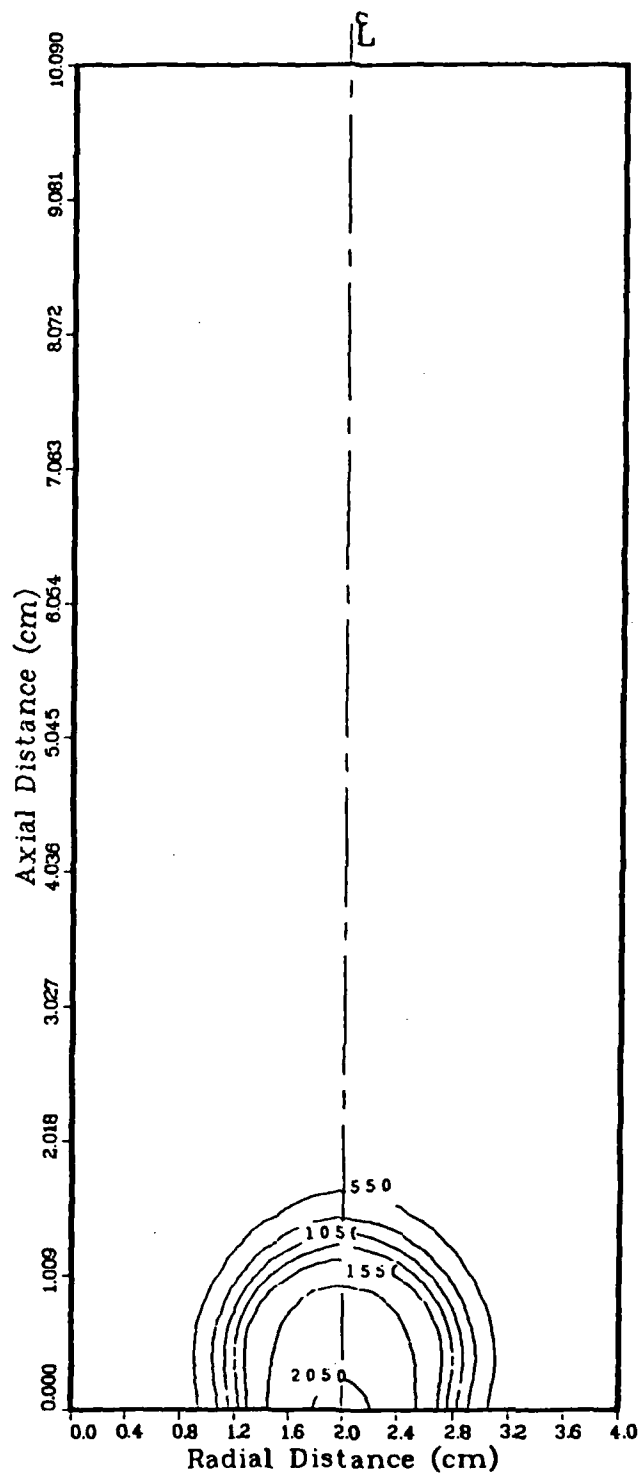Baseline Simulation at 0.2 msec.

39

Figure 8(b). Temperature Distribution (°K) for the Baseline Simulation at 0.2 msec.
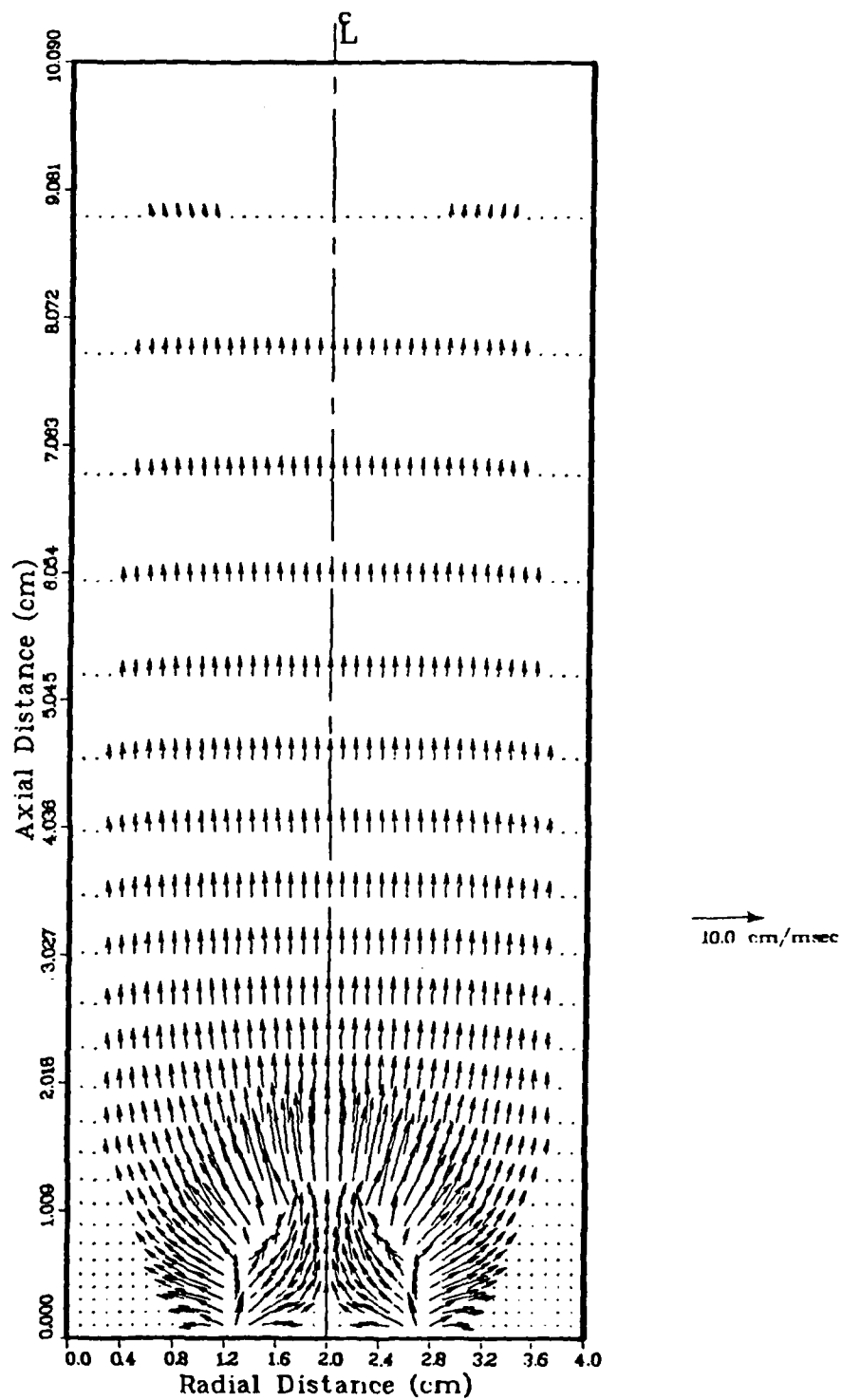
40

Figure 8(c). Velocity Vector Plot for the Baseline
Simulation at 0.2 msec.
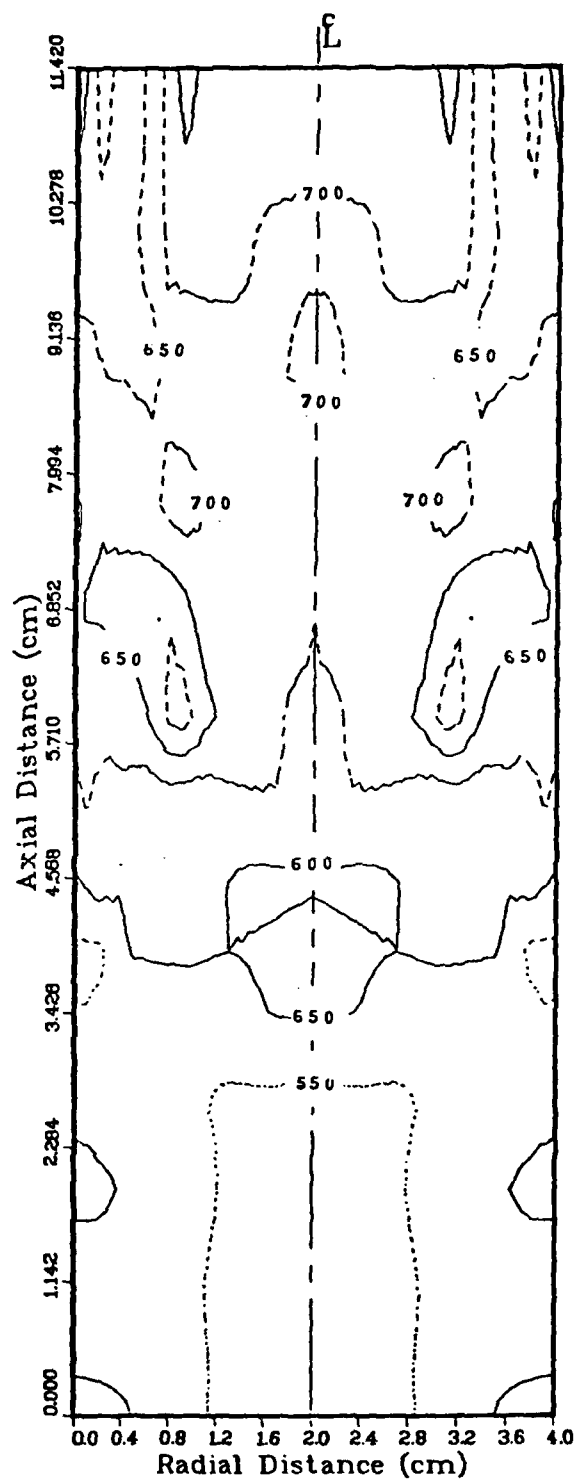
Figure 9(a).   Pressure Distribution (MPa) for the
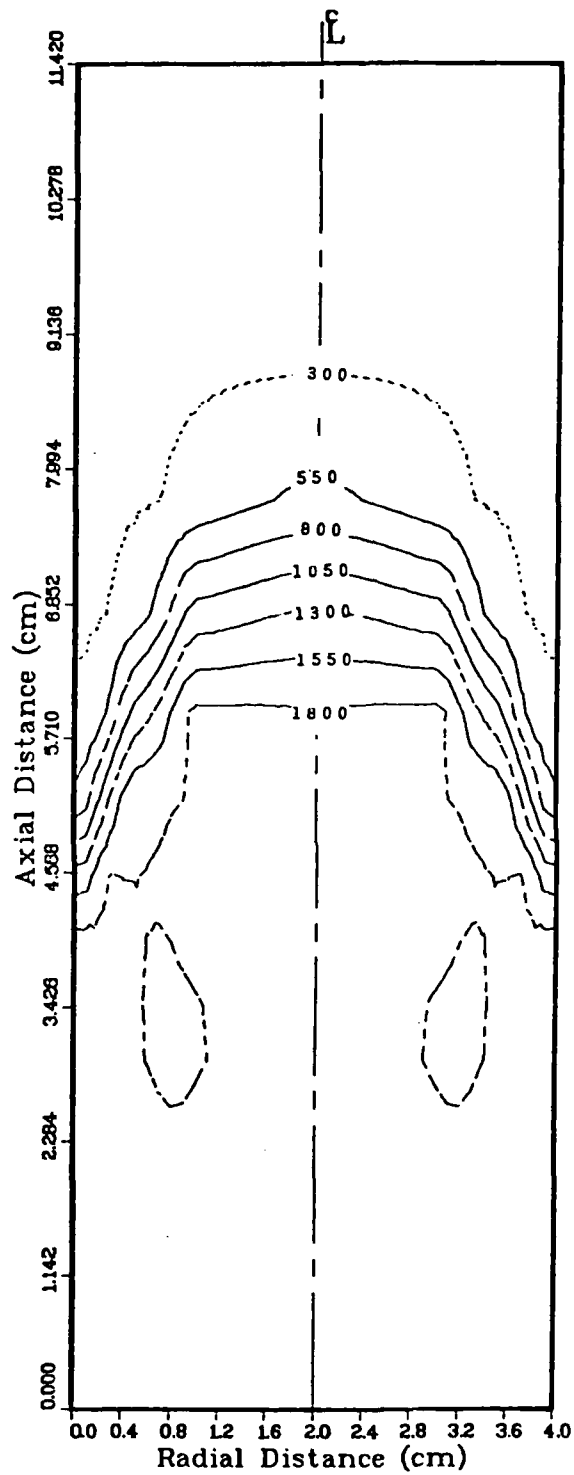Baseline Simulation at 0.4 msec.

42

Figure 9(b).   Temperature Distribution (°K) for the
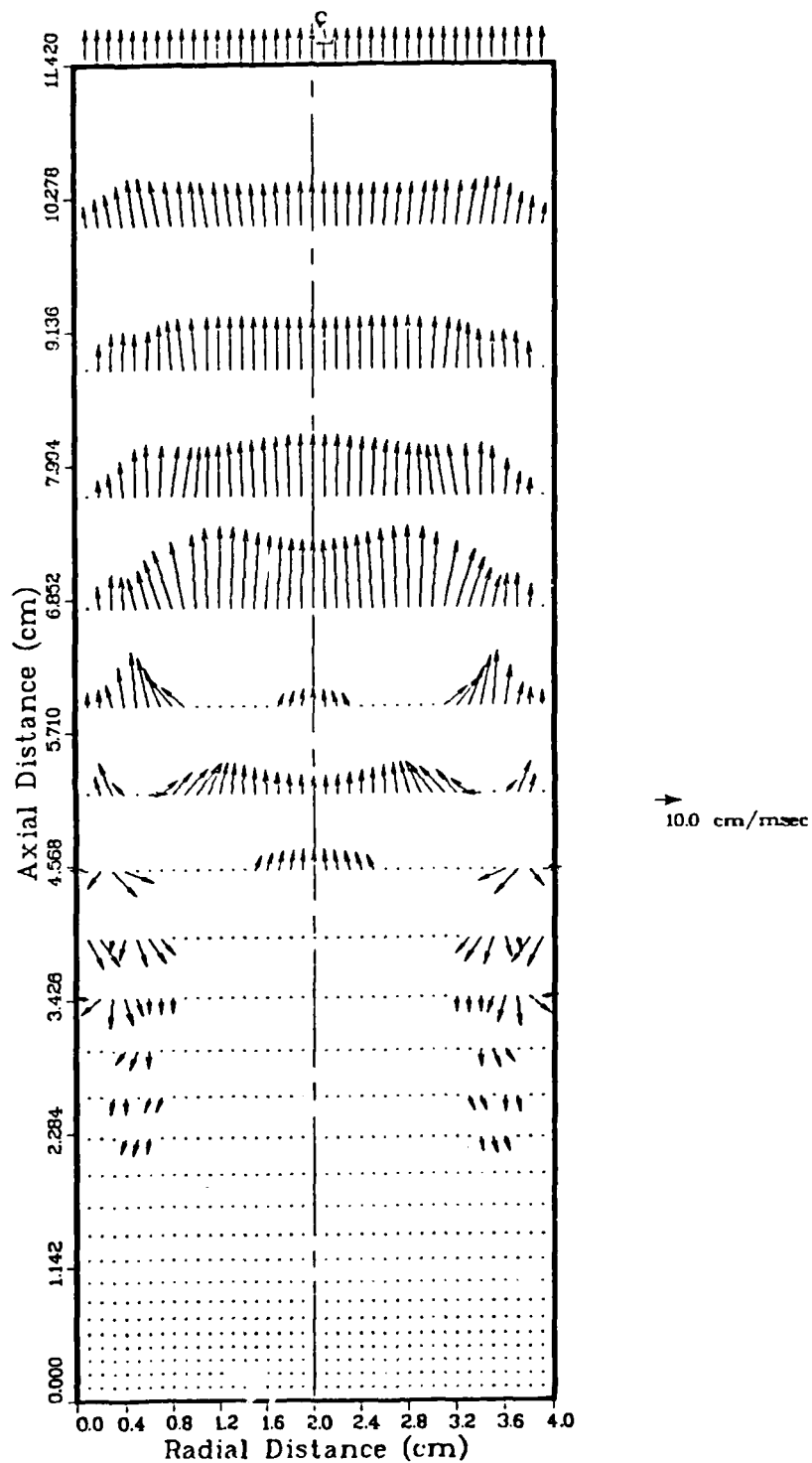Baseline Simulation at 0.4 msec.

43

Figure 9(c). Velocity Vector Plot for the Baseline
Simulation at 0.4 msec.

44
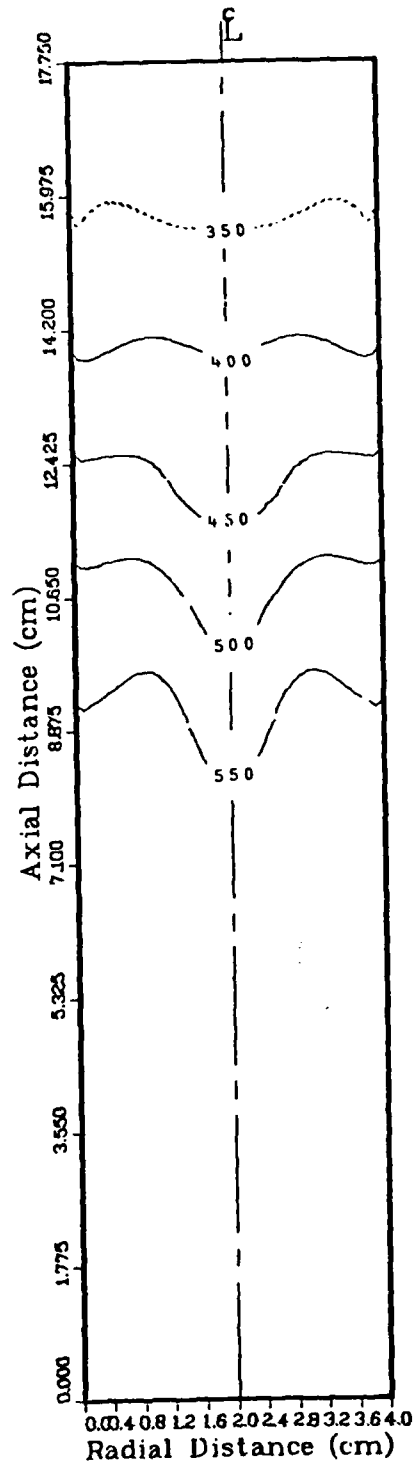
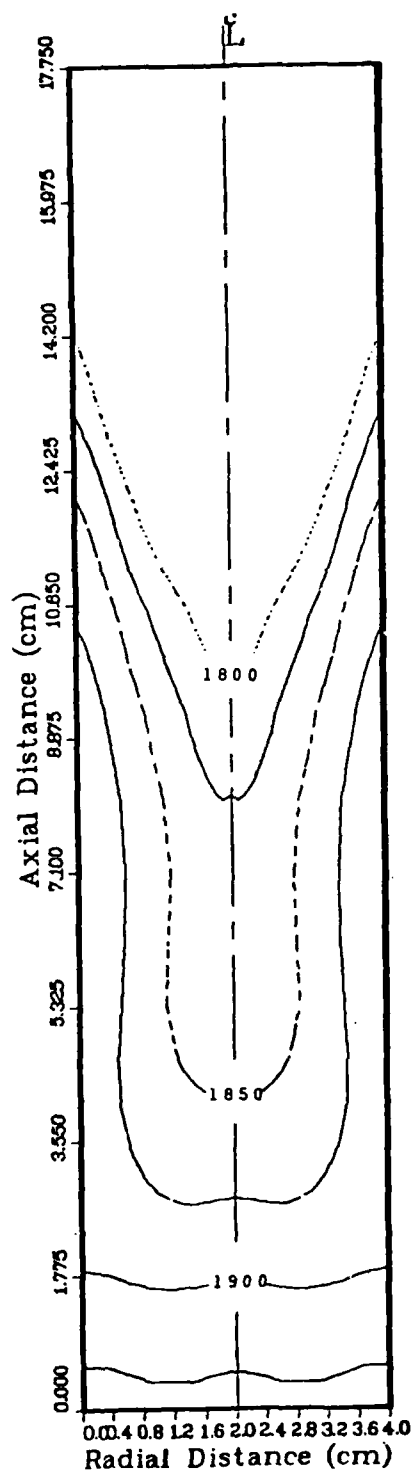Figure 10(a). Pressure Distribution (MPa) for the Baseline Simulation at 0.6 msec.

Figure 10(b).   Temperature Distribution (°K) for the
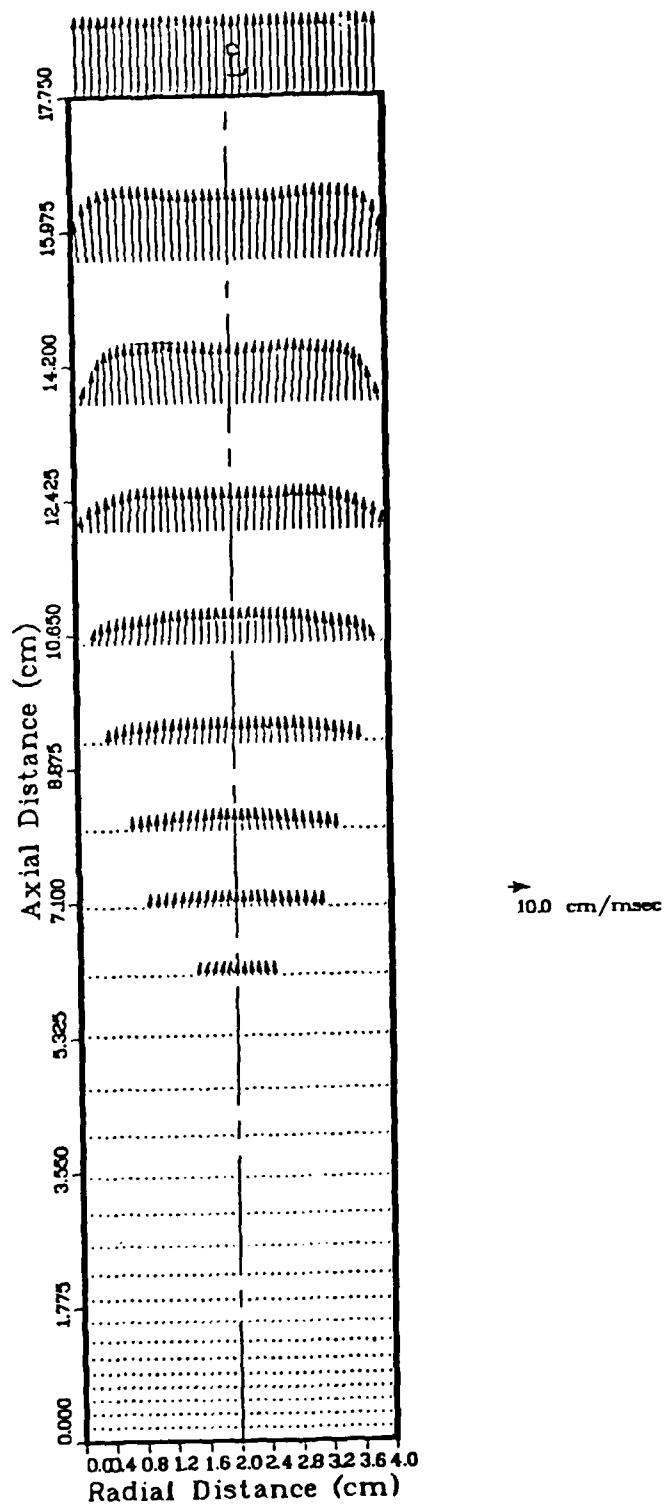Baseline Simulation at 0.6 msec.

46

Figure 10(c). Velocity Vector Plot for the Baseline
Simulation at 0.6 msec.

does not assure that the detailed thermal and fluid mechanical processes occurring within the combustion chamber are necessarily properly characterized. As an aid to understanding the details of the flow structure, these processes may be visualized via contour and velocity vector plots at specified times during the firing cycle. Figures 8 through 10 display the detailed flowfield results for the baseline simulation at 0.2, 0.4 and 0.6 msec. In each case, Figures (a) represent contour plots of pressure distribution within the combustion chamber, while Figures (b) display chamber isotherm lines, and Figures (c) show the resultant fluid motion via velocity vector plots. The velocity vector plots were generated using a minimum velocity cut-off specified to be 15% of the maximum velocity at each specified time. Those velocities below the cut-off limit are represented in these plots by a dot rather than an arrow.

Figure 8 displays pressure, temperature, and velocity results at the time of ignition cut-off (0.2 msec). Figure 8(a) shows the pressure distribution within the chamber at rather coarse contour intervals. At these coarse intervals the pressure profiles are shown to be nearly planar. This of course will not be true in the ignition region as indirectly shown in the velocity vector plot, Figure 8(c). The figure does, however, indicate the increase in pressure throughout the chamber at this time. While the figure represents only a snapshot of the pressure distribution, it is apparent that compression waves are being generated as the gas cavity expands and is reflected in the fall-off in pressure with axial distance from the breech end. It should also be noted that the acoustic wave propagation speed in the liquid propellant is on the order of 200 cm/msec which translates to a wave traverse time of 0.05 msec based on a chamber length of 10 cm.

Figure 8(b) shows the development of the temperature field at 0.2 msec. The formation of a slightly ellipsoidal gas cavity can be seen in this figure with peak gas temperature on the order of 2050°K. In this figure, as well as all isotherm plots to follow, the pure liquid/gas interface coincides approximately with the 550°K isotherm. Thus, this isotherm may be used to trace the development of the gas cavity. In Figure 8(b) the position of the 550°K isotherm indicates that the gas cavity extends approximately 1.5 cm in the axial direction with a maximum extent in the radial direction of approximately 1.1 cm. The slower growth in the radial direction is due to the close

48

proximity of the chamber wall. Finally, the peak temperatures shown in this figure are somewhat lower than the equilibrium temperature of $2342^\circ K$ obtained in constant volume bomb simulations using the same chemistry model and reflects the expansion of the gas due to slight liquid compression and the motion of the projectile.

Figure 8(c) shows the resultant fluid motion at this time. As noted in this figure, maximum velocities are obtained at the liquid/gas interface and are directed normal to the interface. The gas motion within the cavity reflects the slightly ellipsoidal shape of the gas cavity. Flow outside the cavity region is directed axially toward the projectile peaking along the axis and falling off toward the wall as a wall boundary layer is developed. At this early time the cavity interface is moving at a substantially higher speed than the projectile as reflected by the lack of velocity vectors at the projectile base (the projectile velocity is less than 15% of the maximum flow velocity). Finally, it should be noted that the flow nearest the projectile has a slight radial motion as a result of the viscous nature of the fluid.

Figure 9 displays the pressure, temperature and velocity fields at 0.4 msec. The simple pressure profiles shown in Figure 8(a) have now been replaced by a rather complex pressure field at 0.4 msec (Figure 9(a)). While Figure 8(a) had indicated a relatively one-dimensional pressure field, Figure 9(a) shows the two-dimensionality which becomes apparent at later times. While this figure is again a snapshot in time, it is apparent that complex wave interactions are taking place with relative maximums occurring at several locations within the field. Comparison of this figure with the velocity results shown in Figure 9(c) tends to indicate that a compression wave train of sufficient magnitude to cause flow reversal in certain regions of the flowfield is propagating towards the breech end. Overall pressures as shown here are considerably higher than those found at the earlier time and coincide approximately with peak pressures as indicated in Figure 7. Finally, the spatial variations shown in the pressure field at 0.4 msec tend to explain the oscillations about the mean pressure as shown in Figure 7 as well as many experimental pressure-time traces.

Figure 9(b) displays isotherm lines in the chamber at this time. The gas cavity is now seen to occupy a substantial portion of the chamber with the flame front extending to the chamber wall. Here, as in the previous temperature plot, the $550^\circ K$ isotherm line defines the boundary between the pure liquid

49

and the gas cavity. The burnout to the wall which is shown here (but which is not borne out in experimental data) is principally the result of the use of a constant eddy viscosity assumption, as will be shown later in this discussion. Finally, peak temperatures are lower than those indicated earlier, which reflects further gas expansion due to the motion of the projectile.

The velocity vector plot for 0.4 msec, Figure 9(c), shows that the location of the peak fluid motion remains at the flame front with the gas cavity continuing to overtake the projectile. Motion behind the leading edge of the cavity is diminished with flow reversal noted further back in the cavity region. This flow reversal is caused by opposing compression waves. The exact cause of the variation in flow direction in this reversal region is difficult to determine from analysis of this one instant in time, but appears to be caused in part by interactions of the wave with the wall. Ahead of the interface the flow is nearly planar with some boundary layer influences apparent near the chamber wall where a tendency toward vortical motion can be noted. Finally, the projectile base is shown in this figure to have advanced 1.42 cm with the projectile having attained a velocity of 16 cm/msec.

The final set of plots to be considered for the baseline simulation are shown in Figure 10. Figure 10(a) presents the pressure distribution within the chamber at 0.6 msec. The liquid propellant has been totally consumed by this time and the drop in peak pressure is a reflection of the pure expansion process now taking place. The curvature of the isobars in this figure is due to the viscous nature of the fluid. Figure 10(c) shows that the boundary layer thickness grows from the projectile base towards the breech end. This thickening boundary layer is reflected in the increase in curvature of the pressure isobars in this direction. The decrease in pressure at the chamber wall is a consequence of the mass deficit which develops along the wall due to the motion of the projectile which must be made up by a radial flow from the core region toward the wall. The effects of viscosity are repeated in the isotherm plot shown in Figure 10(b). The total energy is relatively constant throughout a chamber cross-section while the flow as shown in Figure 10(c) attains a maximum at the cylinder axis and decreases to zero at the wall. Thus, isotherm lines will dip and reach a minimum at the axis with a corresponding maximum at the chamber wall. The motion within the fluid at this time is influenced mostly by rarefaction rather than compression waves and the resultant flow

50

is shown in Figure 10(c). As was noted earlier, some tendency toward radial flow is noted near the projectile base with a tendency towards vortical motion exhibited along the chamber wall. The projectile acceleration over this 0.2 msec time period is shown to have increased dramatically with the projectile having moved 7.75 cm down the barrel, attaining a velocity of 45 cm/msec.

The baseline simulation is a clear indication of the utility of the LPG model developed during the course of this investigation. As has been shown here, good agreement is obtained for pressure-time trace data as compared with experimental measurements. The results of the baseline simulation, while encouraging, have also raised some interesting questions. For example, an indication of deficiencies in the current calculation lies in the fact that while good pressure-time trace comparisons were shown, relatively flat flame fronts are predicted. This is in contradiction to X-ray photographs and other indirect evidence which indicates that an annulus of propellant remains to burn out last. An investigation of this observation was undertaken to help understand how the coupling of the fluid dynamics and chemistry affects the detailed flame structure.

To assess the influence of turbulent mixing assumptions on the shape of the flame front, a simple, but more realistic, variable eddy viscosity prescription was implemented to replace the constant eddy viscosity assumption employed in the baseline simulation. The variable eddy viscosity prescription is based on a simplification of the Prandtl mixing length model, in which the local eddy viscosity is made dependent only upon the local flow speed. This variable eddy viscosity is defined so as to have roughly the same average value as the constant viscosity used in the baseline simulation. With the exception of the eddy viscosity, all other parameters remained the same as those used in the baseline simulation.

An isotherm plot at 0.4 msec for this simulation is shown in Figure 11 in comparison with the 0.4 msec isotherm plot for the baseline case. Strikingly different profile shapes can be observed. First, and most notable is the fact that the flame front does not reach the chamber wall in the variable eddy viscosity simulation. (The 550°K isotherm has been highlighted here to accentuate the liquid/gas interface.) Second, cavity growth along the axial direction has been retarded with the leading edge not quite extending
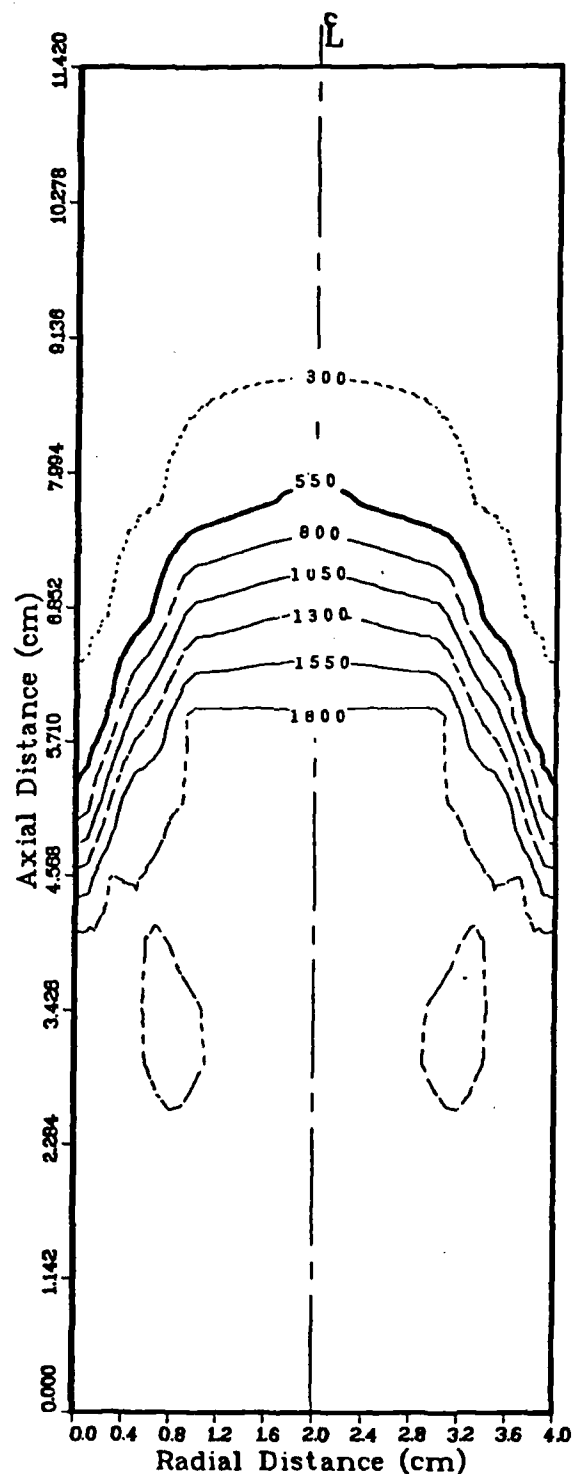
51

Figure 11(a). Temperature Distribution (°K) for the Baseline Simulation (Constant Eddy Viscosity) at 0.4 msec.
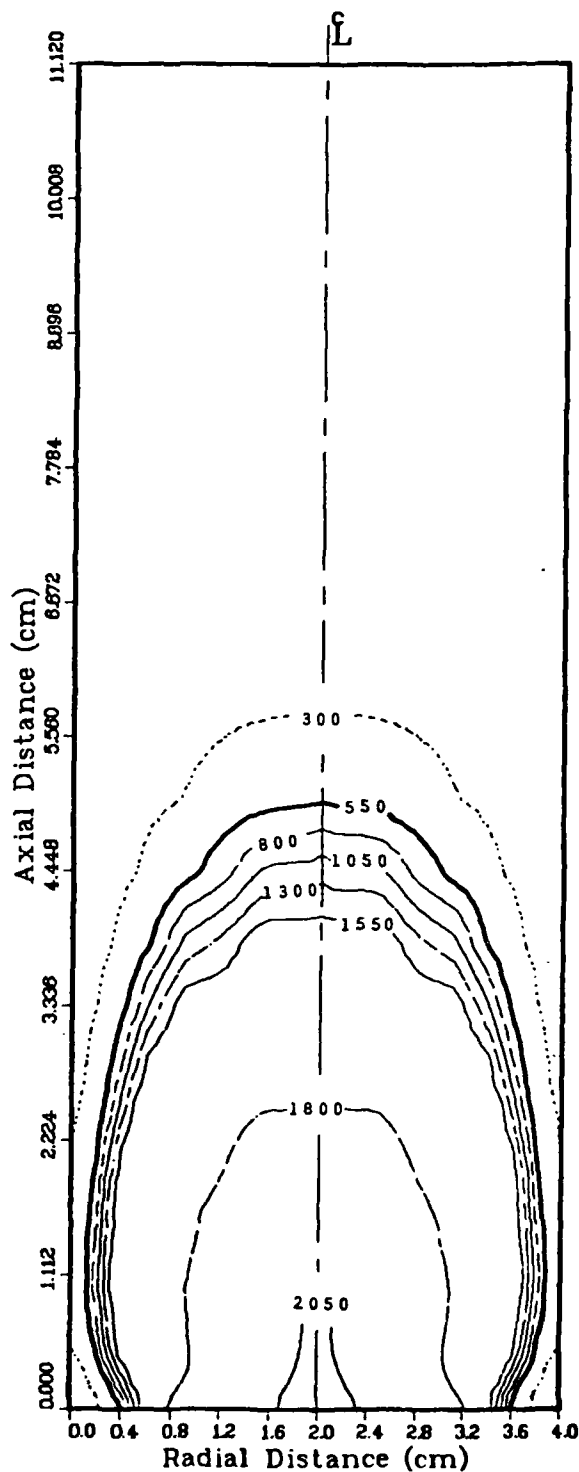
Figure 11 (b). Temperature Distribution (°K) for the Variable Eddy Viscosity Simulation at 0.4 msec.

halfway down the chamber. Third, a pocket of residual liquid propellant remains near the breech-wall corner where flow speeds are a minimum. The presence of a liquid annulus and the occurrence of a fluid pocket about the breech end chamber wall have been noted in experimental firings. The fact that the model is able to predict these phenomena with a more physically correct turbulence prescription is a promising step in the modeling development effort directed towards a more accurate treatment of the turbulent mixing process. Caution, however, must be interjected at this point. It would not be proper to assume that this simple turbulence prescription is sufficient for an accurate description of the mixing process at the flame interface and the subsequent flame propagation. Further quantification of the parameters governing mixing at the interface is needed as well as additional development of the modeling of the highly coupled chemical processes taking place. This need for additional model refinement is shown by the results displayed in Figures 12 and 13. These results include both baseline and variable viscosity breech end ignition cases and also computations, to be discussed below, of a projectile base ignition case. Substantially different pressure-time traces result from the breech-end ignition variable viscosity simulation, when compared with the results of the baseline case. Although the baseline pressure trace data agreed well with the experimental test data, the corresponding pressure trace data showed marked differences with experimental results. This lack of agreement between the two simulations points out that, while it is necessary for pressure-time traces to agree with experimental data, this agreement is not sufficient to conclude that the predicted flow within the combustion chamber corresponds to that which is occurring in actual gun firings.

To conclude the preliminary model assessment, it is appropriate to consider a simulation in which an entirely different flow pattern is generated. For this purpose it was decided to investigate an LPG firing in which a projectile base igniter was used. Problem parameters remained identical to those used in the baseline simulation with the exception of two modifications. The axial variation in zone size was reversed from that employed in the baseline simulation, and ignition at the projectile was treated by a source deposition along the first row of zones adjacent to the base and extending radially outward 0.4 cm. Total energy deposited within this region was chosen to agree with that used in the baseline simulation and the
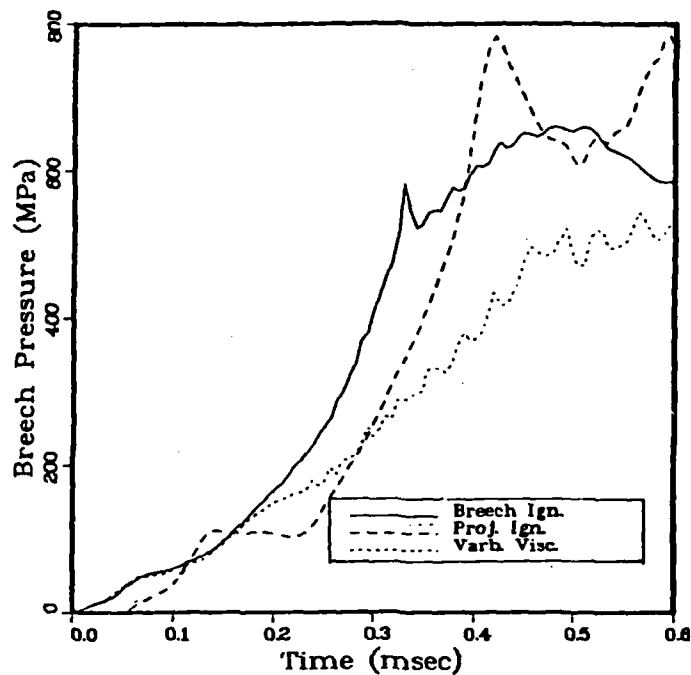
Figure 12(a). Breech End Pressure-Time Trace Comparing the
Baseline, Variable Viscosity Breech End
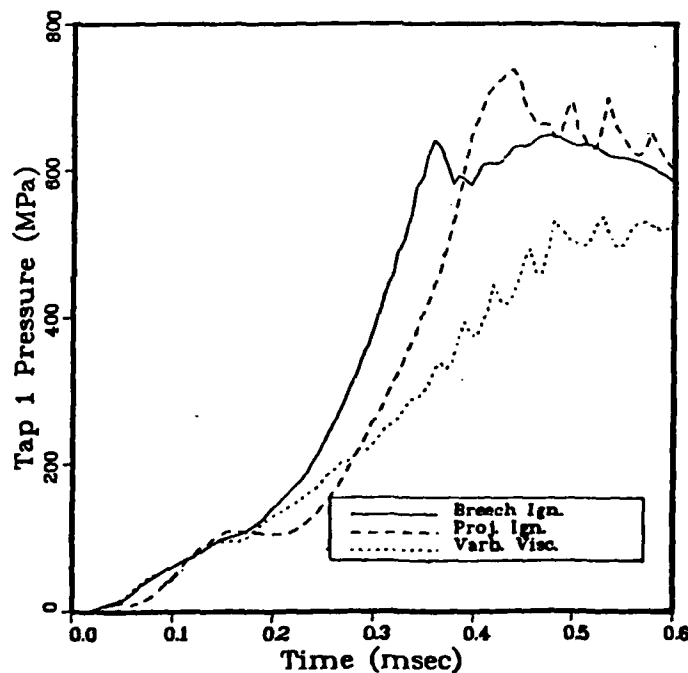Ignition and Projectile Base Ignition
Simulations.

Figure 12(b). Tap 1 (3.2 cm From Breech End) Pressure-Time
Trace Comparing the Baseline, Variable
Viscosity Breech End Ignition and Projectile
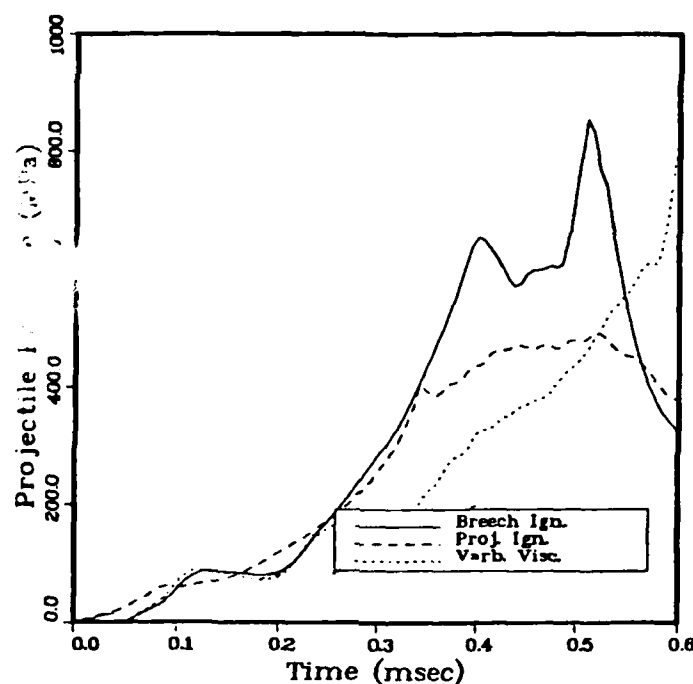Base Ignition Simulations.

54

Figure 13(a).   Projectile Base Pressure-Time Trace
Comparing the Baseline, Variable
Viscosity Breech End Ignition and
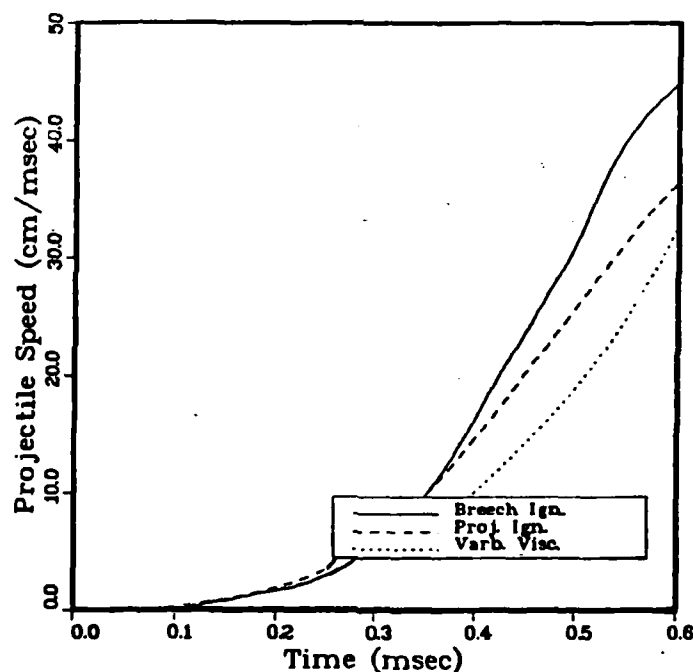Projectile Base Ignition Simulations.

Figure 13(b).   Projectile Speed-Time Trace Comparing
the Baseline, Variable Viscosity
Breech End Ignition and Projectile
Base Ignition Simulations.

same parabolic time profile for source deposition was imposed. Time history comparisons of this simulation with the baseline case are shown in Figures 12 and 13 and the associated details of the flowfield at 0.4 msec are shown in Figure 14.

Figures 12 and 13 display time traces of the pressure at three locations along the chamber as well as a projectile velocity history. Referring to Figures 12(a) and 13(a), it is apparent that the projectile base trace for the projectile base ignition [Figure 13(a)] has the same qualitative shape as the breech end trace for the breech end ignition [Figure 12(a)]. However, some quantitative differences are apparent. For example, peak pressures for the projectile base ignition [Figure 13(a)] are substantially lower than those shown in Figure 12(a) for the breech end ignition. Further, the first pressure peak occurs later in time for the projectile base ignition case than for the baseline simulation. These differences are due to the motion of the projectile which acts to relieve the pressure build-up within the ignition region, retarding the advance of the flame front because of the reduced rate of reaction at the lower pressure levels. The lower pressures exhibited in the projectile base ignition simulation directly affect the advancement of the projectile and lower projectile speeds are noted in Figure 13(b).

The existence of lower pressures within the chamber is further demonstrated in the 0.4 msec isobar plot shown in Figure 14(a). Here peak pressures are on the order of 600 MPa, which may be compared with peak pressures of 700 MPa as shown in Figure 9(a) for the baseline simulation. Again the isobar plot indicates a highly two-dimensional flow with pressure maximums occurring off-axis near the flame front. These pressure peaks appear to be the result of the interaction of an incident pressure wave with the liquid/gas interface. Variations in both flow direction and magnitude occur within this region as shown in Figure 14(c). Figure 14(b) displays the distribution of temperature at this same time. Again the $550^{\circ}K$ isotherm may be used to delineate the liquid gas interface. As was shown previously for the baseline simulation, burn-through to the wall has occurred, although slightly more cavity curvature is apparent here when compared with the baseline simulation, Figure 9(b). In addition, the flame front progression down the barrel is retarded from that which was shown in the baseline case. Again this is due to the more direct relief of pressure buildup through the motion of the projectile that occurs since inertia of the liquid does not have to be overcome.
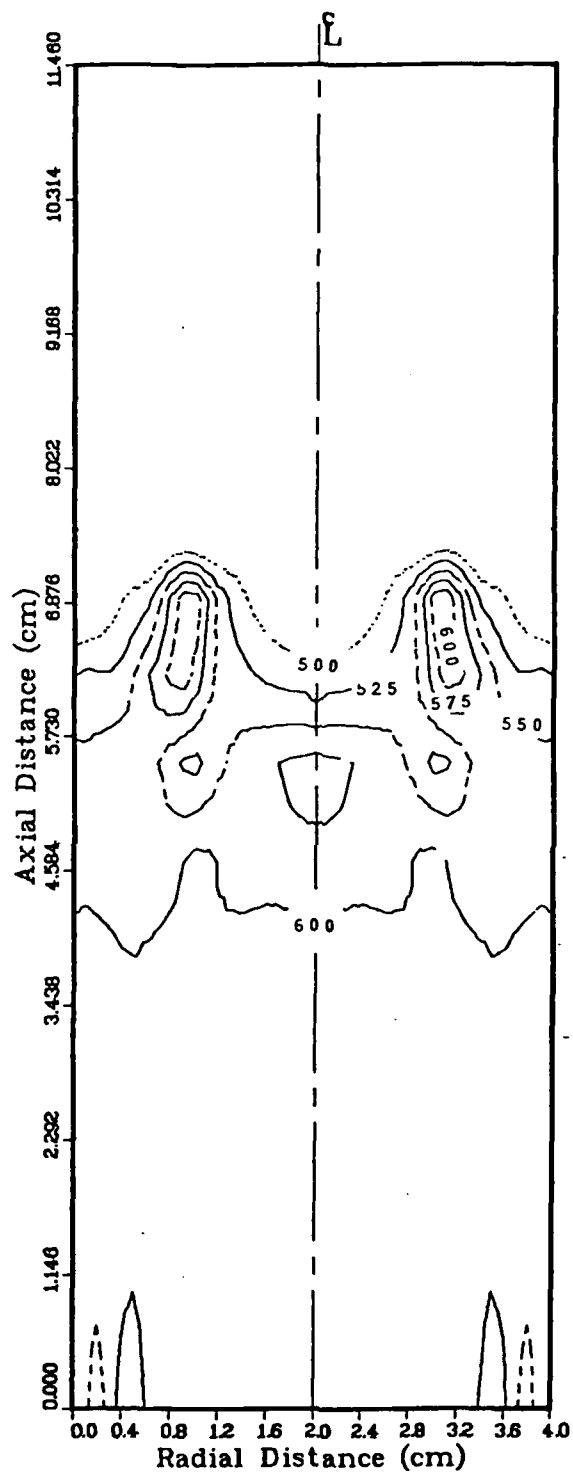
56

Figure 14(a).   Pressure·Distribution (MPa) for the
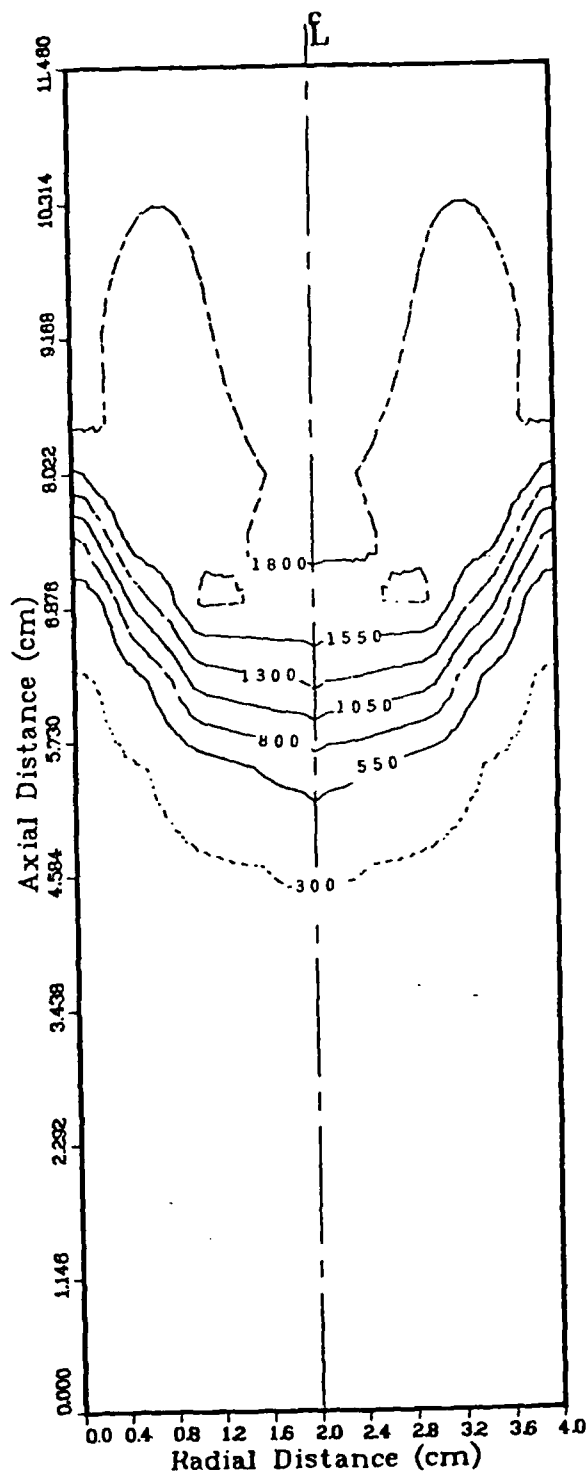Projectile Base Ignition at 0.4 msec.

57

Figure 14(b).   Temperature Distribution (°K) for the
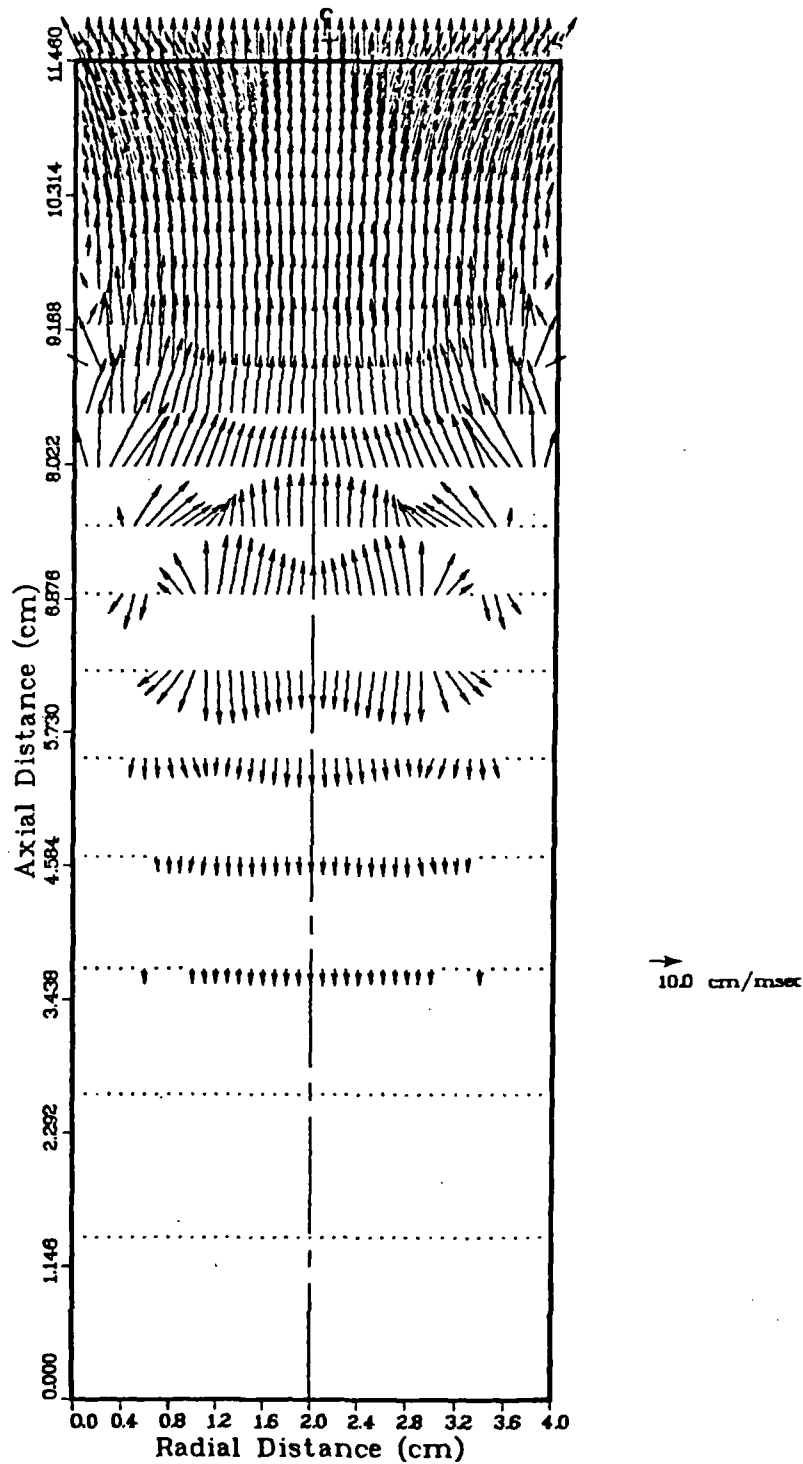Projectile Base Ignition at 0.4 msec.

Figure 14(c).   Velocity Vector Plot for the Projectile
Base Ignition at 0.4 msec.

59

Figure 9(c) displays the flowfield for this case at 0.4 msec. Within the gas cavity the flow is directed toward the projectile while near the liquid/gas interface the flow is seen to reverse as the liquid ahead of the flame front is displaced towards the breech end. This breech end flow is rapidly reduced due to the nearly incompressible nature of the liquid while some vortical motion of the fluid is noted near the projectile at the chamber walls. A consequence of this time-dependent, non-uniform flow is the development of large shear and pressure forces in the neighborhood of the liquid/gas interface. These predicted results quantify the potential importance of droplet formation due to the disruption of the liquid/gas interface caused by these forces.

In order to provide some additional insight relative to the effects of droplet formation on the combustion process a study was undertaken to include droplet processes within the current theoretical framework. Equations 10 - 12 and 15 with the boundary conditions given in Table III were used. The rate of droplet generation was taken to be proportional to the velocity difference across the liquid/gas interface, which is consistent with the Helmholtz relationship, Eq. 21. The rate of droplet consumption was assumed proportional to the drop surface area. Dynamic equilibrium for both convective and turbulent transport of the droplets was also assumed. The formulation was implemented for parametric studies on the effect of droplet size. Figure 15 shows that the generation of 10 μm drops can significantly increase the rate of pressure rise relative to the case with no drops present. A higher peak pressure and larger amplitude oscillations are also observed with drops present. Figure 16 shows that the gas density and drop size distribution is radially non-uniform with the bulk of the droplets concentrated near the gas-liquid interface. Since the transport of drops by turbulence as well as by convection is taken into account, these results indicate that the drops are rapidly consumed giving rise to the steep pressure-time trace shown in Figure 15. Excessively steep pressure rises have been observed in experimental gun firings. While the research conducted to date indicates that vapor phase chemical kinetics and homogeneous mixing rates account, at least in part, for this behavior, these studies illustrate that droplet formation and consumption should also be considered in more detail. This should include dynamic and thermal non-equilibrium in the characterization of the spray dynamics. In addition, drop size distribution effects should be included to properly describe the sensitivity of drop consumption to the drop size.
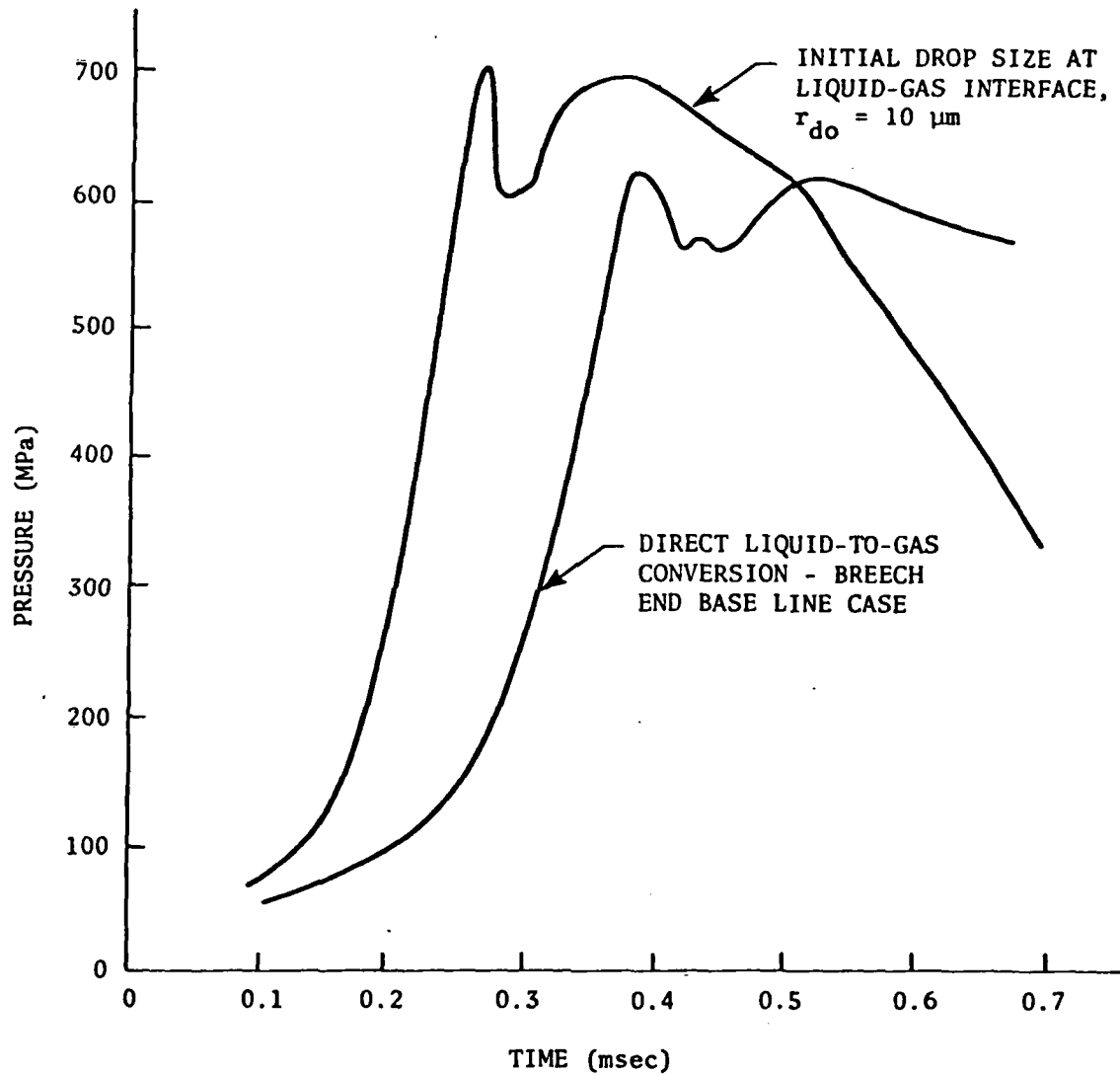
60

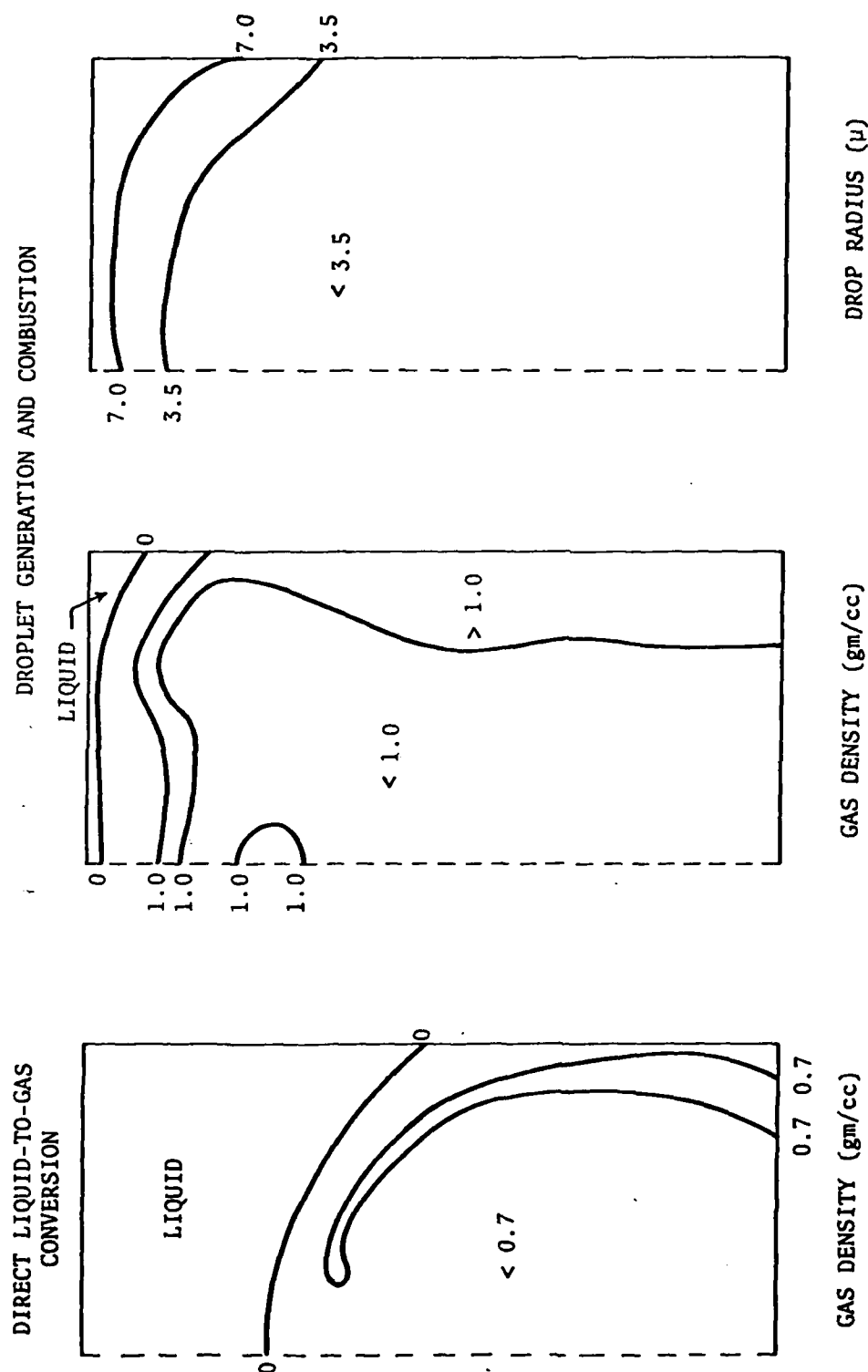Figure 15. *The Effect of Drop Formation and Consumption - Pressure/Time Trace.*

61

Figure 16. Effect of Drop Formation and Consumption - Gas Density and Drop Size Distribution Contours.

Conclusions

A model framework to treat transient multiphase reacting flow of the type encountered in liquid propellant guns has been developed.

A preliminary applications of the model to a 1D transient gas gun, the Lagrange problem, and to several configurations of the 2D LPG problem have shown the following:

- The present model and the attendant numerical solution of the model equations reproduce an analytic solution for the Lagrange problem. While a favorable comparison with a flow having an analytic solution is necessary, it is cautioned that this does not constitute validation particularly for the far more complex flowfield encountered in the LPG where several characteristic length and time scales are encountered.

- Application of the model to LPG configurations shows that depending upon the respective rates of turbulent transport and chemical reaction, the combustion process can quench or occur at extremely high rates. Sensitivity to both mixing and kinetic rates is demonstrated by these predictions.

- A favorable comparison between predictions and data from a test firing has been obtained. The data comprised a pressure-time history while the predictions included a full description of the flowfield.

- The potential importance of drop formation, transport, and consumption has been shown by comparing LPG combustion for direct liquid-to-gas conversion with droplet formation and consumption. More rapid burning and larger pressure oscillations are predicted with droplet combustion.

Analysis of predicted flowfield details shows a relatively flat predicted flame zone leaving no annulus of unburnt propellant prior to complete propellant burnout. This prediction is contrary to X-ray photographs that do show an annulus of propellant. However, calculations made with a more realistic locally flow dependent eddy diffusivity showed that this assumption, while degrading the pressure-time comparison with data, dramatically changed the computed shape of the flame front and produced a cavity

63

with an annulus of propellant. This result demonstrates the need to be cautious in the interpretation of model predictions based on a single comparison using pressure data alone. While agreement with measured pressure is necessary, it is not sufficient to guarantee that other potentially critical details are adequately characterized.

These results indicate that in addition to pressure measurements, visual information is extremely valuable in providing semi-quantitative data on the structure of the combustion process. Ultimately, quantitative measurements in this extremely hostile environment would be invaluable.

REFERENCES

1. Comer, R. H., R. B. Shearer, and R. N. Jones, Interior Ballistics of Liquid Propellant Guns (U), Ballistic Research Laboratory, Report 1205, 1953 (Secret).

2. Edelman, R. B., The Interior Ballistics of Liquid Propellant Guns, R&D Associates, RDA-TR-4400-010, August 1974.

3. Erickson, Alve, Interior Ballistics of Liquid Propellant Guns, Foster-Miller Associates, Inc., Final Report (Contract N00123-73-0278), September 1973.

4. Burnett, W. M., An Interior Ballistics Model for Liquid Propellant Guns, Naval Ordnance Station Report IHTR 444, September 1976.

5. Edelman, R. B., P. T. Harsha, and H. D. Hogge, "Analysis of the LPG Combustion Process," 12th JANNAF Combustion Meeting, Naval War College, August 1975.

6. Edelman, R. B., and H. D. Hogge, "A Transient Quasi-One-Dimensional Model of the Interior Ballistics Process for Non-Hypergolic Liquid Bi-Propellant Guns," RDA TR-8700-001, September 1976.

7. Phillips, G., Murty, S., Traci, R., and Edelman, R. B., "Analysis of Interior Ballistics Processes of Bulk-Loaded Liquid Propellant Guns," Proceedings 17th JANNAF Combustion Meeting, CPIA Publication 329, Vol.II, Chemical Propulsion Information Agency, Nov. 1980, pp. 403-448.

8. Boni, A. A., R. M. Traci, S. S. Murty, "Numerical Simulation of Internal Combustion Engine Flows: I. Development and Testing," SAI Report No. SAI-80-509-LJ, DOE Contract No. ET-78-C-03-2089, September 1980.

   Traci, R. M., S. S. Murty, C. W. Wilson, A. A. Boni, "Numerical Simulation of Internal Combustion Engine Flows: II. Turbulence, Swirl Development and Testing," SAI Report No. SAI-80-510-LJ, DOE Contract No. DE-AC03-79ET15397, September 1980.

9. Powell, E. G., et al., "Equations of State and Thermodynamic Data for Interior Ballistics Calculations," Interior Ballistics of Guns, Progress in Astronautics and Aeronautics, Vol. 66, AIAA.

10. Ingraham, R. L., "Is There a Helmholtz Mixing Coefficient?," Los Alamos Scientific Laboratory, Report No. 1593, September 1953.

11. Birkhoff, G., "Taylor Instability and Laminar Mixing," Los Alamos Scientific Laboratory, Report Nos. 1862 and 1927, 1955.

12. Birkhoff, G. and E. H. Zarantonello, "Jets, Wakes and Cavities," Academic Press, Inc., New York, 1957.

13. Edelman, R. B. and P. T. Harsha, "Some Observations on Turbulent Mixing With Chemical Reactions," Progress in Astronautics and Aeronautics, Vol. 58, Turbulent Combustion, Edited by Lawrence Kennedy, AIAA, NY, 1978.

14. Launder, B. E., Morse, A., Rodi, W., and Spalding, D. B., "The Predictions of Free Shear Flows - A Comparison of the Performance of Six Turbulence Models," Free Turbulent Shear Flows Vol. I - Conference Proceedings. NASA SP321, 1973, pp. 361-426.

15. Kuo, T. -W. and Bracco, F. V., "On the Scaling of Transient Laminar, Turbulent, and Spray Jets," SAE Technical Paper Series, Paper No. 820038, February 1982.

16. Hanjalic, K., Launder, B. E., and Schiestel, R., "Multiple Time Scale Concepts in Turbulent Transport Modeling," Second Symposium on Turbulent Shear Flows, Imperial College, London, July 1979.

17. Fabris, G., Harsha, P. T., and Edelman, R. B., "Multiple Scale Turbulence Modeling of Boundary Layer Flows for Scramjet Applications," NASA CR 3433, May 1981.

18. Rodi, W., "The Prediction of Free Turbulent Boundary Layers by Use of a Two-Equation Model of Turbulence," Ph.D. Thesis, University of London, 1972.

19. Sindir, M. M., and Harsha, P. T., "Assessment of Turbulence Models for Scramjet Flowfields," NASA CR 3643, November 1982.

20. Klein, Nathan, "Summary of the JANNAF Workshop on Liquid Propellants for Gun Applications," Fourteenth JANNAF Combustion Meeting, Vol. II, pp. 1-14, Colorado Springs, August 1977.

21. Love, A. E. H. and F. B. Pidduck, "Lagrange's Ballistics Problem," Phil. Trans. of the Royal Society, Vol. 222, 1922, p. 168.

22. Amsden, A. A. and C. W. Hirt, "YAQUI: An Arbitrary Lagrangian Eulerian Computer Program for Fluid Flow at All Speeds," LA-5100, March 1973.

23. O'Rourke, P. J. and T. D. Butler, "June Progress Report 1976: LPG Simulations," Naval Ordnance Station Contract No. MIPR-N00174-4-00025.

ATE
LME